Optical control upon quantum fluids of light

Abstract: Through their extensive study, Bose-Einstein Condensates (BECs) have shown to be an ideal platform for the understanding of many-body physics. On the other hand, quantum fluids of light use photons in the role of bosons and are formally analogue to BECs, thanks to the effective interactions brought by a nonlinear medium. However, their extensive study began only recently and many aspects are still to be understood. In this report I will specifically be interested in the susceptibility of a nonlinear medium (a Rubidium hot vapor) i) to characterise the effective photon-photon interactions, and ii) to study the possibility of adding an optical potential in the system. This work paves the way towards the full control upon quantum fluids of light, with a tunability and repeatability which are key in the perspective of studying many-body phenomena.

Key words: Nonlinear optics, Quantum optics, analogue Bose-Einstein Condensates, Superfluidity

Internship supervised by:
Quentin Glorieux
quentin.glorieux@lkb.upmc.fr / tél.(+33) 1 44 27 41 89
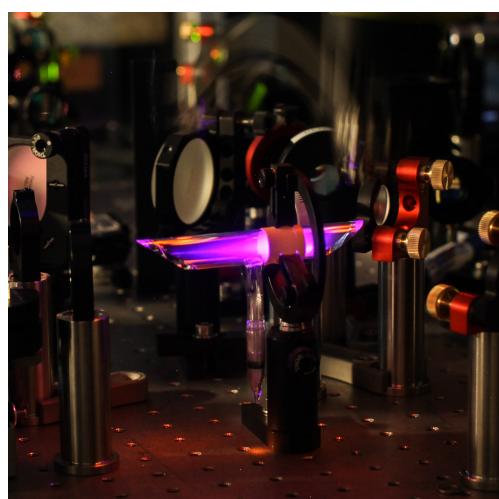
Laboratoire Kastler Brossel
4 place Jussieu, 75005 Paris
http://www.lkb.upmc.fr/

Acknowledgments

Contents

1   Introduction

Nonlinear optics emerged immediately after the invention of lasers, at the beginning of the 60s. Until then, only the linear response of materials had been explored. The generation of high intensity light allowed the observation of nonlinear interactions between photons and dielectric media, one of the most striking effect being the frequency doubling, first showed by Franken et al. (1961).

Besides, the propagation of a laser beam in a Kerr medium is ruled by the well-known nonlinear Schrödinger equation (see for instance Boyd, 2003). The nonlinearity thus acts as an effective photon-photon interaction and the governing equation is analogue to the Gross-Pitaevskii equation (GPE) which describes the dynamics of Bose-Einstein condensates (BECs). Any Kerr medium with a paraxial laser light passing through is therefore a fertile ground to create and study analogue BECs.

I will begin this introduction by describing the physical system I used, along with the main equations, before explaining the fluid of light formalism. This description provides useful physical insights.

1.1   Physical system

Several systems are analogue to atomic BECs, we can mention for instance exciton-polaritons (which are also studied in our group under the supervision of Alberto Bramati). In this set-up however, losses force the cavity to be continuously pumped, and the interaction strength is only slightly tunable (Carusotto and Ciuti, 2013). We thus turn ourselves to Kerr media, and more specifically hot Rubidium vapors, in cavityless cells (like pictured in figure 1.2). This nonlinear medium offers a great playground for the study of analogue BECs: the input state can be chosen almost at will, the interactions are easily and widely tunable through several parameters (laser frequency, temperature of the cell, intensity and waist of the beam) and the visualisation of the output state benefits from highly sensitive optical detection tools.

Let us now detail the equation governing our system and explicit the analogy with atomic BECs (this is done in more details in Fontaine, 2020, chap. 2). We start from two main ingredients: the Maxwell's equations and the polarisability of the media $\mathbf{P}(\omega)$. The latter is centro-symmetric and isotropic, which allows us to write $\mathbf{P}(\omega) = \epsilon_0 \chi^{(1)}(\omega)\mathbf{E} + \epsilon_0 \chi^{(3)}(\omega)\mathbf{E}^3$ by assuming a local response and neglecting for the moment higher order terms (Boyd, 2003). Starting from Maxwell's equations and writing a monochromatic field $\mathbf{E}(\mathbf{r}, t) = \frac{\epsilon}{2}\left(\mathcal{E}_0(\mathbf{r})e^{i(\omega t - k(\omega)z)} + \text{c.c.}\right)$, with ϵ the polarisation unit vector, we obtain after making use of the paraxial and slowly-varying envelope approximations:

$$i\frac{\partial \mathcal{E}_0}{\partial z}(\mathbf{r}_\perp, z) = \left[-\frac{1}{2n_0 k_0}\boldsymbol{\nabla}_\perp^2 - \frac{i\alpha}{2} - k_0\delta n(\mathbf{r}_\perp, z) - \frac{k_0}{2n_0}\chi^{(3)}(\omega)|\mathcal{E}_0(\mathbf{r}_\perp, z)|^2\right]\mathcal{E}_0(\mathbf{r}_\perp, z) . \quad (1.1)$$

This is the well-known NonLinear Schrödinger Equation (NLSE), which describes the evolution of laser light through a nonlinear medium. Let us explain in more details each term on the right-hand side, before illustrating them in figure 1.1:

- $\frac{1}{2n_0 k_0}\boldsymbol{\nabla}_\perp^2\mathcal{E}_0(\mathbf{r}_\perp, z)$: diffraction term, as in the usual paraxial Helmholtz equation $\left(k_0 = \frac{2\pi}{\lambda}\right.$ and $n_0 = \sqrt{1 + \text{Re}\left(\chi^{(1)}\right)}\right)$. The Laplacian only acts in the transverse (x, y) plane.

- $\frac{i\alpha}{2}\mathcal{E}_0(\mathbf{r}_\perp, z)$: linear absorption term, which comes from the imaginary part of the susceptibility, with $\alpha = k_0\, n_0\,\text{Im}\left(\chi^{(1)}\right)$. These are one-photon losses. It is a trade-off necessary to increase the interactions (in our case from getting closer to the atomic resonance, see appendix A).

- $k_0\delta n(\mathbf{r}_\perp, z)\mathcal{E}_0(\mathbf{r}_\perp, z)$: δn is the local variation of the linear refractive index. Its effect is easily understood from geometrical optics where such modulation deviates light rays. This can be seen as an external potential in the transverse plane acting on photons. It is illustrated in figure 1.1a. Unlike in BECs, fluids of light do not require any trapping potential.

- $\frac{k_0}{2n_0}\chi^{(3)}(\omega)|\mathcal{E}_0(\mathbf{r}_\perp, z)|^2\mathcal{E}_0(\mathbf{r}_\perp, z)$: nonlinear term coming from the nonlinear response of the medium (Kerr effect). This creates an effective photon-photon interaction, depending on the sign of $\chi^{(3)}(\omega)$. In practice, a gaussian beam propagating through a nonlinear medium will either focus or defocus (for $\chi^{(3)} > 0$, yielding attractive interactions, or $\chi^{(3)} < 0$, giving repulsive interactions, respectively, see figure 1.1b).

(a) Potential term only


(b) Nonlinear term only
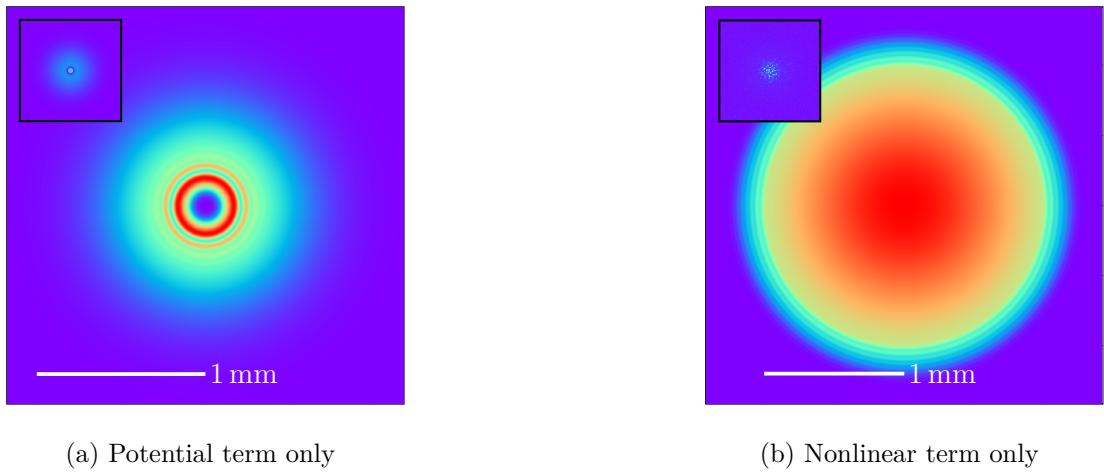
Figure 1.1: Illustrative simulations of the equation (1.1), conserving only the diffraction term and the potential term (a) or the nonlinear term (b). For all the images, we start with a Gaussian beam of waist $0.5\,\mathrm{mm}$ and propagate through a $10\,\mathrm{cm}$ long medium. We add a repulsive gaussian potential, that is with $\delta n < 0$, on (a), while turning off the nonlinearity. This image is thus obtained with geometrical optics. The inset presents the same situation with a potential of opposite sign, which thus guides light. We have no potential in (b), and only a Kerr effect which can either defocus ($\chi^{(3)} < 0$) the beam or focus it ($\chi^{(3)} > 0$, inset) leading to filamentation. In the following we will limit to the case of repulsive potentials and interactions to keep a stable beam.

The equation (1.1) is formally equivalent to the Gross-Pitaevskii equation (GPE) (1.2), with the exception of linear losses. This equation rules the dynamics of BECs, when confined in the third spatial dimension (that is 2D+1 BECs, meaning two spatial and one time dimensions). We indeed retrieve all the terms we have presented above when writing the evolution equation for the wave-function $\boldsymbol{\psi}(\mathbf{r}, t)$:

$$i\hbar\frac{\partial\boldsymbol{\psi}}{\partial t}\left(\mathbf{r}_\perp, t\right) = \left[-\frac{\hbar^2}{2m}\boldsymbol{\nabla}_\perp^2 + V(\mathbf{r}_\perp, t) + g|\boldsymbol{\psi}(\mathbf{r}_\perp, t)|^2\right]\boldsymbol{\psi}(\mathbf{r}_\perp, t)\;,\tag{1.2}$$

with m the boson mass, V an external potential and g the coupling constant. We notice one major difference with the equation (1.1): the derivative on the left-hand side is done according to time in the GPE and according to the propagation axis z in the NLSE. Yet, one can easily map the z axis into an effective time through the following space-time mapping: $z \leftrightarrow \tau = zn_0/c$. Within this picture, the evolution of the electric field along z is a succession of time snapshots, like it is illustrated in figure 1.2. We retrieve with this mapping a 2D+1 evolution.
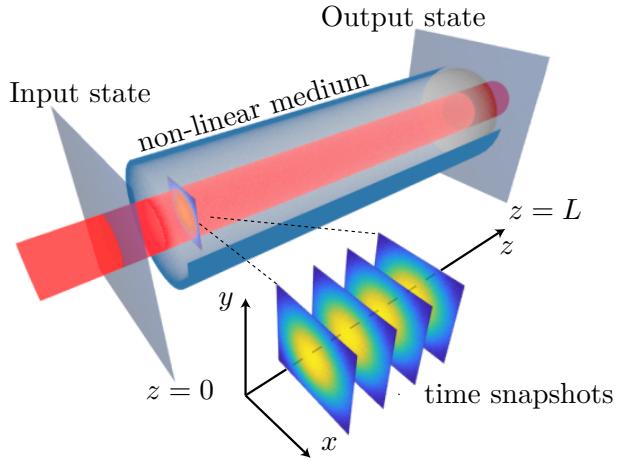
Figure 1.2: Scheme of a nonlinear medium, illustrating the space-time mapping we use to complete the analogy with BECs. Each slice in space corresponds to an effective time, and the evolution occurs through the propagation between the input and output of the cell. We highlight the fact that it is a cavityless medium. The figure is taken from Fontaine et al. (2020).

This mapping uncovers a limitation of our system: we are restricted to the observation of the output of the medium, thus at a time $\tau = Ln_0/c$. This prevents us from studying phenomena developing over long times,

such as thermalisation (only precondensation has been observed, see Šantić et al., 2018). Indeed, phenomena governed by the first term on the right-hand side of the equation (1.1) scale according to z. However, it does not restrict us from observing the nonlinear evolution of the beam, which relies on the last term of the equation (1.1). By rewriting this equation in an adimensionalised form, we obtain that nonlinear effects develop according to z/z_{NL}, with z_{NL} the nonlinear length, (see appendix C and Abuzarli et al. 2021 for instance) which can easily be varied.

1.2 Fluid of light formalism

The NLSE equation (1.1) correctly describes the evolution of the electric field through our medium, yet it provides only little insight to the physics at stake. One can thus reformulate this equation thanks to the Madelung transformation (Madelung, 1926), by writing the electric field $\mathcal{E}_0(\mathbf{r}_\perp, z) = \sqrt{\rho(\mathbf{r}_\perp, z)}\mathrm{e}^{i\phi(\mathbf{r}_\perp, z)}$, with ρ proportional to the light intensity and ϕ the phase of the field. We then obtain:

$$\frac{\partial \rho}{\partial \tau} + \boldsymbol{\nabla}_\perp \cdot (\rho \mathbf{v}) + \alpha \rho = 0 \;, \tag{1.3}$$

$$\frac{\partial \mathbf{v}}{\partial \tau} + (\mathbf{v} \cdot \boldsymbol{\nabla}_\perp)\mathbf{v} = \frac{c^2}{n_0^2}\left[\frac{\tilde{n}_2}{n_0} \boldsymbol{\nabla}_\perp \rho + \frac{1}{2k_0^2} \boldsymbol{\nabla}_\perp \left(\frac{1}{\sqrt{\rho}} \boldsymbol{\nabla}_\perp^2 \sqrt{\rho} \right) \right] \;, \tag{1.4}$$

where we have introduced $\mathbf{v} = \frac{c}{n_0 k_0}\boldsymbol{\nabla}_\perp \phi$ and $\tilde{n}_2 = \frac{1}{2n_0}\chi^{(3)}$. We recognise the Navier-Stokes equations, with equation (1.3) stating the conservation of mass (up to the linear losses) and (1.4) being equivalent to the Euler equation, with ρ acting as a density. This hydrodynamic analogy allows us to visualise a slice of our beam as a "fluid of light", evolving through $\tau \leftrightarrow z$, and whose velocity is determined by the gradient of its phase. This description is very fruitful, and can for instance give rise to turbulence by using two counter-streaming beams (Rodrigues et al., 2020).

The couple of equations (1.3) and (1.4) cannot be solved analytically in general, it becomes thus of particular interest to look at the dispersion relation of our system, which will describe the small density waves propagating on top of a large uniform background. We obtain the Bogoliubov dispersion relation: $\Omega^2 = \frac{|\tilde{n}_2|\rho}{n_0}q^2 + \frac{1}{4k_0^2}q^4$ with q the wavevector of the excitation. The calculations are detailed and the relation is discussed in appendix C. The first observation of this relation in quantum fluids of light has been done by Fontaine et al. (2018), and confirmed recently by Piekarski et al. (2021).

This hydrodynamic analogy underlines that shaping the phase (and thus the velocity) of the fluid at the entrance plane of the nonlinear medium will bring the control upon its propagation, in exactly the same way as a classical fluid. This is particularly easy with our system where the full control of the phase can be achieved with a Spatial Light Modulator for instance. Besides, the interactions are easily tunable: changing the speed of sound or the evolution time L/z_{NL} only requires to vary the laser intensity. With all these ingredients in mind, we can understand that this platform is ideal for the study of analogue BECs, with a very high control of the important parameters and a great repeatability.

During this internship, I aimed at increasing the control we have over this system. This broad goal mainly boils down to the monitoring of the last two terms of equation (1.1). Indeed, the susceptibility of our medium is difficult to characterise completely and no satisfactory theoretical model has been presented in the literature so far.

In section 2 I present two methods which are able to measure the interactions of the medium, and study its variation with the waist of the beam. This is crucial to determine the speed of sound and the nonlinear length of the medium. In section 3 I use these methods to study the transient regime of the susceptibility. This is key in the optics of realising 3D+1 fluids of light.

I then turned to the realisation of an all-optical external potential in section 4, to tune the δn term of equation (1.1). This paves the way toward many experiments requiring a potential, from the probing of superfluidity (section 4.3) which requires a localised defect (i.e. a strong repulsive potential) to optical lattices (section 5.2).

I eventually detail a few promising outlooks that this platforms presents in section 5, from analogue gravity to the realisation of optical lattices and the multiple perspectives it will allow, such as optical band mapping.

2   Control of the interactions

The Kerr medium that I used during this internship is hot Rubidium vapor glass cells. It consists in cavityless cylinder cells (like pictured in figure 1.2), with lengths ranging from 1 to 10 cm, containing Rubidium (Rb). At room temperature Rb is solid and the vapor pressure is small ($N \simeq 10^{15}$ m^{-3}). We can then heat it, thanks to resistors, and tuning the temperature allows us to control the atomic density $N(T)$ of the vapor ($10^{19} - 10^{20}$ m^{-3} in our experiments). It can be changed by several orders of magnitude (the exact formula linking temperature and density is given in Siddons et al., 2008). Hence, this is a key knob to vary the interactions, because $\chi^{(3)} \propto N(T)$ (see appendix A). Besides, Rb has several transitions within the close infrared spectrum, which can be easily addressed with a laser. Controlling the detuning of the laser within a range of several GHz is another crucial parameter to change the photon-photon interactions. Thus, Rb hot vapor cells offer a very convenient Kerr medium, which is easy to handle and with a widely tunable nonlinearity.

2.1   Position of the problem

The propagation of light inside a Kerr medium is controlled by the equation (1.1). Being able to monitor finely each one of the terms would allow us to explore at will a variety of different systems (some examples of which will be detailed in sections 4 and 5). Therefore, a key ingredient in this task is the characterisation of the susceptibility of the medium. The canonical way of measuring a nonlinear index is with the so-called "z-scan" technique (see for instance Sheik-bahae et al., 1989). However, it is only feasible in the case of a thin nonlinear medium, that is when $L \ll z_{\mathrm{R}}$ with L the length of the medium and z_{R} the Rayleigh length of the beam being used. Hot Rubidium vapor cells on the other hand do not fall into this category ($L \sim 10$ cm). Therefore one should adopt other experimental techniques.

An alternative method has been suggested by Callen et al. (1967) and is since used by the fluid of light community (Šantić et al., 2018; Fontaine et al., 2018). It relies on the observation of the far field image of the output of the medium, which presents some characteristics rings (Fontaine, 2020). It is however not very reliable when the accumulated nonlinearity becomes important; that is in our case when the beam self-defocuses. Indeed, at that point the approximation neglecting the diffraction term in (1.1) (see Finot et al., 2018) breaks down and the contrast of the rings lessens such that they become difficult to count. These drawbacks motivated us to develop alternative techniques in order to measure the nonlinear index of our medium. I will present these techniques along with the results we obtained in the following sections.

2.2   Interferometric method

The aim of this method is to retrieve the phase of a beam passing through the cell (signal beam) thanks to a reference beam in a Mach-Zehnder set-up, as illustrated in figure 2.1 (a typical image obtained with the set-up is shown in figure 2.2a). The camera recovers the intensity of the sum of the two electric fields, that is:

$$I_{\mathrm{camera}}(\mathbf{r}) \propto \left| \mathcal{E}_{\mathrm{s}}(\mathbf{r})\, \mathrm{e}^{i(\mathbf{k}_{\mathrm{s}}\mathbf{r}+\varphi(\mathbf{r}))} + \mathcal{E}_{\mathrm{r}}(\mathbf{r})\, \mathrm{e}^{i\mathbf{k}_{\mathrm{r}}\mathbf{r}} \right|^2 = \left| \mathcal{E}_{\mathrm{s}}(\mathbf{r})\, \mathrm{e}^{i\varphi(\mathbf{r})} + \mathcal{E}_{\mathrm{r}}(\mathbf{r})\, \mathrm{e}^{ik_x x} \right|^2 \tag{2.1}$$

$$= \underbrace{I_{\mathrm{s}}(\mathbf{r}) + I_{\mathrm{r}}(\mathbf{r})}_{\text{continuous part}} + \underbrace{n_0 \epsilon_0 c\, \mathrm{Re}\left(\mathcal{E}_{\mathrm{s}}(\mathbf{r})\mathcal{E}_{\mathrm{r}}(\mathbf{r}) \mathrm{e}^{i(\varphi(\mathbf{r})+k_x x)} \right)}_{\mathcal{V}(\mathbf{r})}, \tag{2.2}$$

where we have used the fact that the angle between the two beams is small and k_x is the projection on the x-axis of the wavevector of the reference. $\varphi(\mathbf{r})$ is the phase accumulated by the signal beam, which corresponds to the nonlinear phase plus a constant phase. The two electric fields are linearly polarised in the same direction. The off-axis contribution performs in practice a shift in the Fourier space for the last term of equation (2.2). This can be seen as a kind of heterodyne detection, with the reference beam shifting the frequencies of the signal, and the demodulation being computerised. Therefore, we can obtain all the information on the phase by filtering $\mathcal{V}(\mathbf{r})$ in the Fourier space. Taking the Fourier Transform of this expression (in practice a Fast Fourier Transform) yields:

$$\tilde{I}_{\mathrm{camera}}(\mathbf{k}) = \tilde{I}_{\mathrm{s}}(\mathbf{k}) + \tilde{I}_{\mathrm{r}}(\mathbf{k}) + n_0 \epsilon_0 c\, \mathcal{TF}\left(\mathcal{E}_{\mathrm{s}} \mathrm{e}^{i\varphi(\mathbf{r})} \right)(\mathbf{k}) * \left(\mathcal{TF}\left(\mathcal{E}_{\mathrm{r}} \right)(\mathbf{k} - \mathbf{k_x}) + \mathcal{TF}\left(\mathcal{E}_{\mathrm{r}} \right)(\mathbf{k} + \mathbf{k_x}) \right), \tag{2.3}$$

where "~" means the Fourier transform of a quantity, "$*$" denotes a convolution product and $\mathbf{k_x} = (k_x, 0)$. In practice, the reference beam is a large in size (compared to the signal) gaussian beam and the convolution
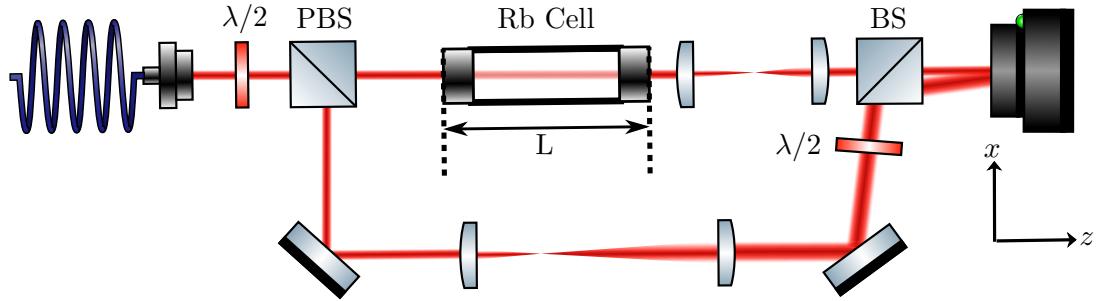
Figure 2.1: Scheme of the experimental set-up allowing the phase retrieval. The output plane of the cell is imaged on the camera thanks to a $4f$ telescope. The signal beam is then recombined with a tilted reference (the angle is exaggerated).

product mainly acts as an offset which creates two satellite peaks on both sides of the continuous part. It becomes easy to filter out one peak, as can be seen in figure 2.2b. Taking the inverse Fourier Transform of one satellite peak immediately yields half of $\mathcal{V}(\mathbf{r})$. By taking its argument, we recover:

$$\Phi(\mathbf{r}) = \varphi(\mathbf{r}) + k_x x = \underbrace{\varphi_{\mathrm{NL}}(\mathbf{r})}_{\text{nonlinear phase}} + \overbrace{\varphi_0}^{\text{geometrical phase}} + \underbrace{k_x x}_{\text{off-axis contribution}} . \tag{2.4}$$

The aim is then to retrieve the nonlinear phase from the total phase. We proceed in two steps:

- the off-axis contribution is removed by subtracting the mean gradient of the phase. Indeed, the nonlinear phase has a zero mean gradient due to the geometry of the beam.

- we get rid of the constant phase by identifying the phase of low intensity points (that is far from the center of the beam), where the nonlinear phase is barely above zero.

(a)

(b)
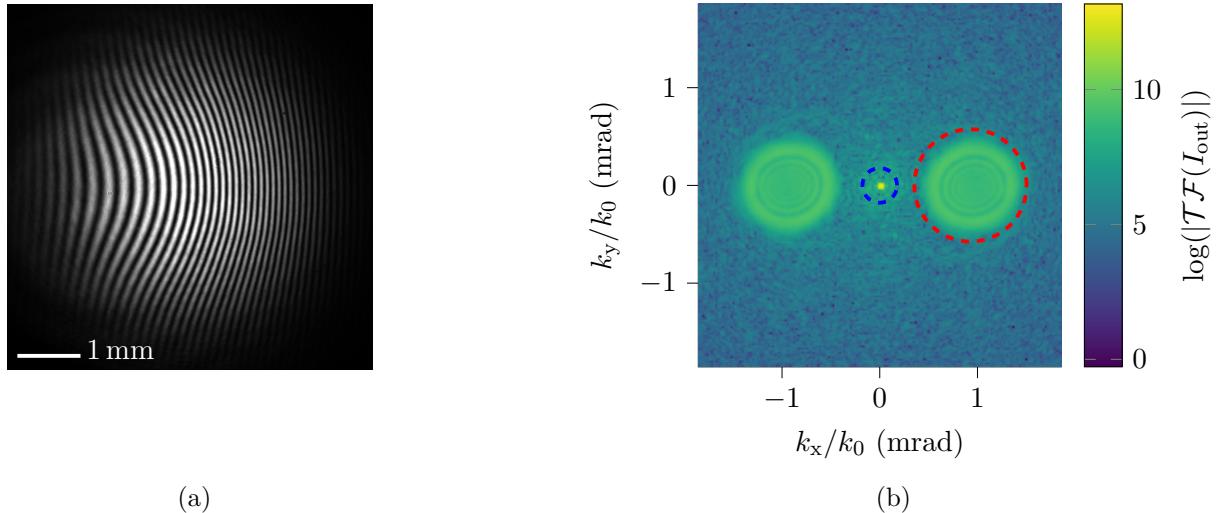
Figure 2.2: (a) Example image obtained by the Mach-Zehnder set-up. The curvature of the fringes is due to the nonlinear phase accumulated by the signal beam. (b) corresponding 2D FFT, cropped to better see the three peaks. The FT of $\mathcal{V}$ is circled by the red dashed line and the FT of the continuous signal by the blue dashed one. We select the red dashed peak and perform its inverse FT to retrieve the phase of (a). Using the blue dashed continuous part as well allows us to obtain the visibility of the interferogram.

We then recover the phase of the beam at the output of the cell, which allows us to measure precisely the nonlinear phase accumulated by the beam due to the propagation in the cell. On the other hand, we have by definition of the nonlinear phase:

$$\varphi_{\mathrm{NL}}(\mathbf{r}) = k_0 L \, \Delta n = k_0 L \, n_2 \frac{1}{L} \int_0^L I(z, \mathbf{r}) \, \mathrm{d}z , \tag{2.5}$$

where L is the length of the cell, Δn the nonlinear change of refractive index and $n_2 = \frac{1}{\epsilon_0 n_0 c}\mathrm{Re}\left(\chi^{(3)}\right)$. We note that all the quantities we observe are integrated over the cell, as we image the output plane only. In a first approximation, $I(z, \mathbf{r}) = \exp(-\alpha z)I(0, \mathbf{r})$, taking only the linear absorption into account and neglecting the effect of defocusing. Therefore:

$$\varphi_{\mathrm{NL}}(\mathbf{r}) = k_0 L\, n_2 I(0, \mathbf{r})\frac{1 - \mathrm{e}^{-\alpha L}}{\alpha L} \ . \tag{2.6}$$

However, the equation (2.6) is only valid at low power because it does not take into account the saturation of the medium (see appendix A) neither the defocusing of the beam, which can change its intensity profile. In order to overcome these problems, we introduce another quantity: the saturation intensity. Looking only at the center of the beam, we have:

$$\Delta n = \frac{n_2 \tilde{I}}{1 + \tilde{I}/I_{\mathrm{sat}}} \ , \tag{2.7}$$

where $\tilde{I}$ is the intensity at the center of the beam integrated over the cell and the denominator comes from the infinite expansion of the nonlinear susceptibility (see appendix A). By performing a ramp of intensity and collecting $\varphi_{\mathrm{NL}}(\mathbf{r} = 0)$ for each picture, we recover n_2 and I_{sat} by fitting the measurements, like it is shown in figure 2.3a. Our system offers several tuning parameters which can change the nonlinear index: temperature of the cell, detuning and waist of the beam. The figure 2.3b presents the variation of n_2 according to the waist. This variation is caused by the finite transit time of atoms through the beam, as explained in appendix A. This is crucial to bear this in mind in our experimental setup: at a fixed intensity, the speed of sound as well as the evolution length will vary by changing the waist of the beam.
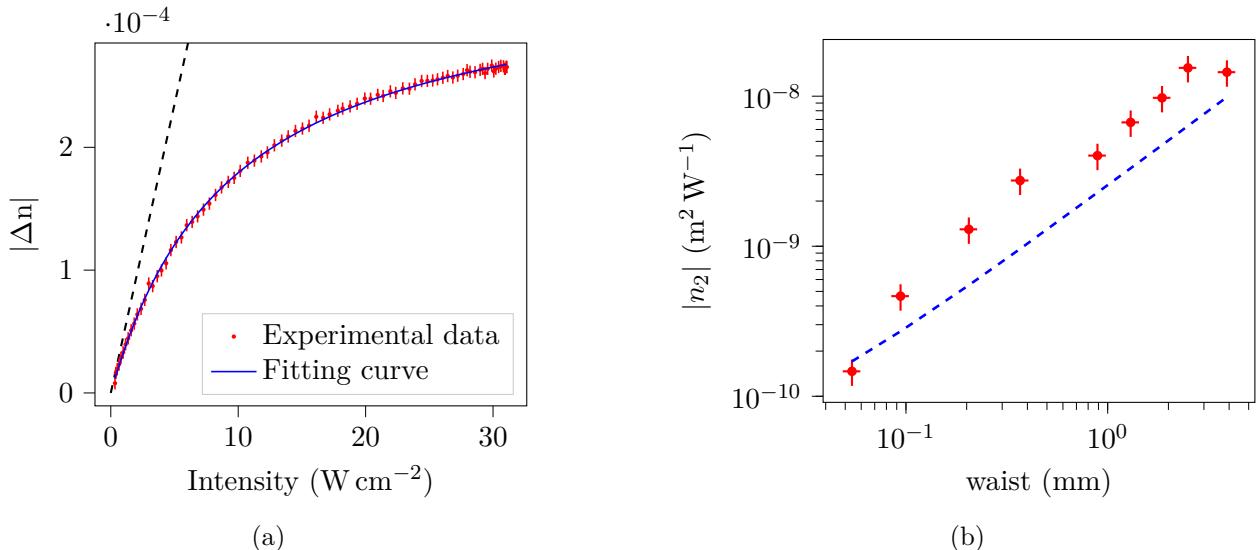
Figure 2.3: (a) Measure and fit of the nonlinearity of the medium by performing a ramp of intensity. The fit yields $I_{\mathrm{sat}} = 7.4\,\mathrm{W\,cm^{-2}}$ and $n_2 = 4.7 \times 10^{-9}\,\mathrm{m^2\,W^{-1}}$. The dashed line corresponds to the initial slope, that is the value of n_2. Note that we will always deal with $\Delta n < 0$, that is repulsive interactions. (b) presents n_2 measurements for different waists. We observe no saturation of n_2 with the size of the waist, which is in agreement with the model developed in appendix A. It yields the dashed blue line with *no adjustable parameter* (note that for each point in (b) we have a saturation of Δn, but we present here only the initial slopes, that is n_2). Parameters: $T = 433\,\mathrm{K}$ and $\Delta = -4.0\,\mathrm{GHz}$.

One has however to be careful with the values of I_{sat} given by the fit. First, it includes here a dependence on the detuning: $I_{\mathrm{sat}} = I_{\mathrm{sat},\Delta=0}(1 + (\Delta/\gamma)^2)$ (with Δ the detuning and γ the total decay rate, see appendix A). Besides, the fitting value we recover is not that of the atomic susceptibility only, as it incorporates the geometrical dilution of intensity due to the beam defocusing. The fitting saturation intensity is therefore an effective value aggregating the atomic one and the contribution of the defocusing. This method allows nonetheless the retrieval of the nonlinear refractive index value: it corresponds to the slope of the curve in figure 2.3a when $I \ll I_{\mathrm{sat}}$, where the fit is analytical.

2.3   Density method

An alternative method to measure the nonlinear index of our medium is to take advantage of the defocusing of the beam. The method is simple: one performs an intensity ramp, captures the intensity profile at the output of the cell and calculates for each image the quantity $\langle R^2 \rangle$ defined by the equation (D.2). It quantifies the mean spreading of the beam and corresponds to w_0^2 in the case of a Gaussian beam. As a centered and normalised Gaussian curve can be entirely defined by its variance, it seems reasonable to characterise the shape of a defocusing beam with one number only.

The calculations supporting this method, made by Nicolas Pavloff, are detailed in appendix D. Knowing the waist of our beam, the propagation length and the transmission through the cell there are only two free parameters left to propagate the equation (1.1): n_2 and I_{sat}. However, the analytical formula given in section D breaks down when $I \simeq I_{\text{sat}}$. The only way to measure n_2 and I_{sat} is thus to fit the data with numerical simulations of the propagation equation (1.1), like it is done in figure 2.4. This method allows us to retrieve the saturation intensity, contrary to the interferometric method. Indeed, the "geometric saturation" brought by defocusing is taken into account by the simulation of the propagation. The figure 2.4 presents a set of data of $\langle R^2 \rangle$ taken with a ramp of intensity, and these values are fitted to obtain n_2 and I_{sat}. The interferometric method yields similar values: n_2 values fall within 5 % of each other, and the I_{sat} ones within 12 %. As expected, I_{sat} with this second method is higher because it doesn't incorporate the "geometric saturation" from the defocusing which we are not able to take into account with the interferometric method.
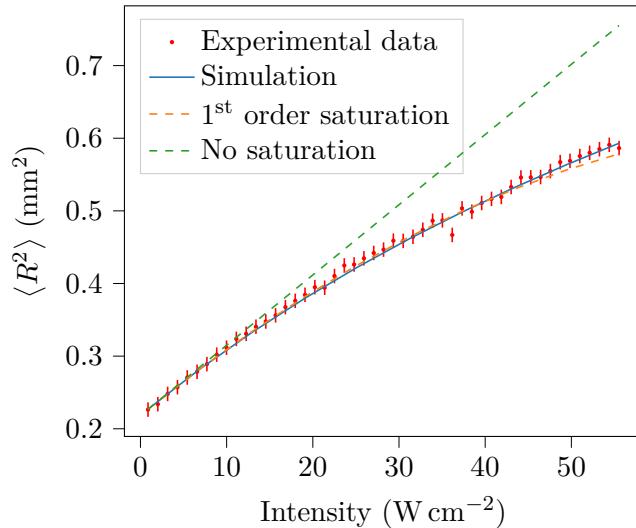
Figure 2.4: Comparison between the experimental (dots), analytical (dashed lines) and simulated (solid lines) values of $\langle R^2 \rangle$. The simulation yields $I_{\text{sat}} = 75\,\text{W}\,\text{cm}^{-2}$ and $n_2 = 2.3 \times 10^{-9}\,\text{m}^2\,\text{W}^{-1}$. The agreement between analytical and simulated values is good (within 3 %) thanks to the intensity staying below I_{sat}. Analysing the same data set with the interferometric method gives: $I_{\text{sat}} = 67\,\text{W}\,\text{cm}^{-2}$ and $n_2 = 2.2 \times 10^{-9}\,\text{m}^2\,\text{W}^{-1}$.

However, this method presents a major drawback: the beam must change size during the propagation in order to have an accurate measurement of the nonlinear index. For the data of figure 2.4, it is increased by 75% for the higher intensity (defining the size as $\sqrt{\langle R^2 \rangle}$). Yet, as seen in figure 2.3b, the nonlinear index varies with the beam size. The measure we obtain is thus that of a mean nonlinear index integrated along the cell and we are not able explore the dependence of the nonlinear index on the waist, which is crucial in our experiments where we vary the waist from one dataset to another.

We have presented in this section two methods to retrieve the nonlinear index of our medium:

- an interferometric method, which retrieves the phase of the beam at the output of the cell. One can then obtain the nonlinear index from a fit by performing a ramp of intensity.

- a density method, which only looks at the intensity of the output plane. A ramp of intensity is once again mandatory to fit any curve to the data.

Both methods are accurate to obtain n_2, as it is extracted from the low-intensity images. At higher intensity however, both methods have flows: the interferometric method underestimates I_{sat} whereas the density method becomes unreliable due to the change of waist through the propagation.

Measuring the nonlinearity of our medium is crucial: in our experiments the speed of sound is given by $c_{\text{s}} = \sqrt{\Delta n}$, and it plays a major role in nearly all the experiments (to calculate the Mach number in section 4 for instance). In the following we will thus prefer the interferometric method for one main reason: it immediately yields Δn for each image (no fit is required as we are not interested in this case in the value of n_2 and I_{sat}), whereas for the density method Δn is obtained from numerical simulations only.

3   Pulsed fluid of light

The fluid of light system is analogue to 2D+1 Bose-Einstein Condensates as we have seen thanks to equation (1.1), where we have considered a continuous wave electric field. A pulsed electric field would modify this equation by introducing a temporal derivative of the field as follows (Larré and Carusotto, 2015):

$$i\frac{\partial \mathcal{E}_0}{\partial z} = -\frac{1}{2k_0}\nabla_\perp^2 \mathcal{E}_0 + \frac{D_0}{2}\frac{\partial^2 \mathcal{E}_0}{\partial t^2} - k_0\frac{\delta n(\mathbf{r}, t)}{n_0}\mathcal{E}_0 - \frac{k_0\chi^{(3)}(\mathbf{r}, t)}{2n_0^2}|\mathcal{E}_0|^2\mathcal{E}_0 \ , \tag{3.1}$$

where D_0 is the Group Velocity Dispersion (GVD), and we placed ourselves in the reference frame moving at the group velocity of the field. By rescaling the time axis, it is then possible to recast this equation into a 3D+1 GPE equation, in a similar way that equation (1.1) is equivalent to the 2D+1 GPE equation. Note that it requires a mapping of the time coordinate onto a third spatial dimension. It is thus possible to have analogue 3D+1 BECs by using pulsed beams. Another important feature of this equation is the temporal dependence of the susceptibility (it can be retrieved from the Optical Bloch Equations, see appendix A and figure 3.5). A pulsed fluid of light would explore the transient regime of the susceptibility of the medium, which can change drastically from its steady-state value. Being able to measure the susceptibility in the transient regime is therefore a key step towards the control of 3D+1 fluids of light. I will explore in this section a way to measure the nonlinear susceptibility of our medium in the transient regime.

3.1   Contrast rings

The first step in studying the transient regime is to pulse our beam. Thus, we place an Acousto Optic Modulator (AOM) before the cell, which is used as a shutter by selecting only the first diffracting order of the AOM. It can be switched on and off in less than 50 ns, which makes it a very convenient tool to obtain pulses of light of a given duration. By then using the set-up pictured in figure 2.1, we obtain an interferogram (such as the one in figure 3.1a). However, the contrast varies with the radius of the beam to form what I will denote as "contrast rings".

Where do these rings come from? During the propagation through the cell, the pulse gains a nonlinear phase as we have seen in section 2. However, the nonlinear phase accumulated at the front of the pulse is not the same as the one at the back of the pulse: the susceptibility of the medium changes along the pulse. The interferogram thus varies continuously between the beginning and end of the pulse, and the whole pulse is integrated by the camera, blurring the contrast in this peculiar way. Conducting 2D+1 NLSE simulations for different susceptibilities and summing the resulting fields in order to mimic our imaging system yields similar interferograms.

Even though these contrast rings seem to contain information about the transient regime, it is not satisfying because of the integration of the pulse on the camera. We therefore develop another set-up to avoid this inconvenience.

3.2   Experimental set-up

The main difficulty in studying the transient regime of the susceptibility comes from the fact that a camera is needed in order to retrieve the nonlinear phase (with the methods given in section 2). It is therefore limited

(a)

(b)
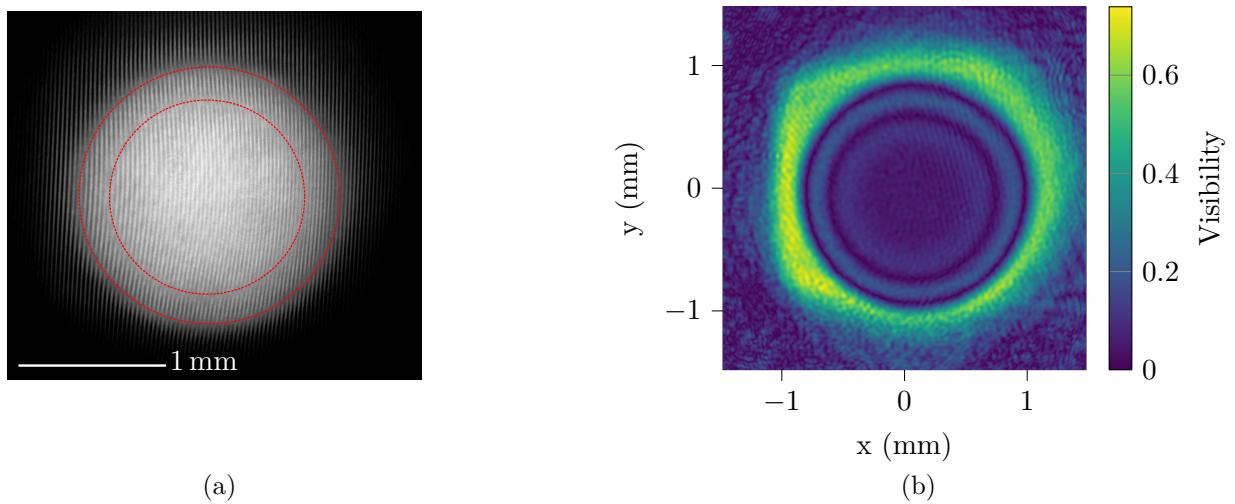
Figure 3.1: (a) Inteferogram of a pulsed beam. Two contrast rings are visible, and highlighted here by red-dotted lines. Extracting the visibility with the method explained in section 2 yields the figure (b), where the two contrast rings are visible.

to a temporal resolution of a hundred Hertz at most. This is way too slow to capture the temporal response of the medium which we expect to be in the range from kHz to MHz (the natural linewidth of the transition is 6 MHz). A more complex set-up, detailed in figure 3.2, is needed: the reference beam, which was pulsed the same way as the signal beam in section 3.1 is now shorter, thanks to a second AOM. In the recombination of both pulses right before the camera, the interferences are then contained in a certain time-window (see figure 3.3a). Therefore, we retrieve the phase from a small temporal part of the pulse only. Changing the delay between the two pulses eventually leads to the knowledge of the transient nonlinear phase across the whole signal pulse with a temporal resolution only limited by the duration of the reference pulse.
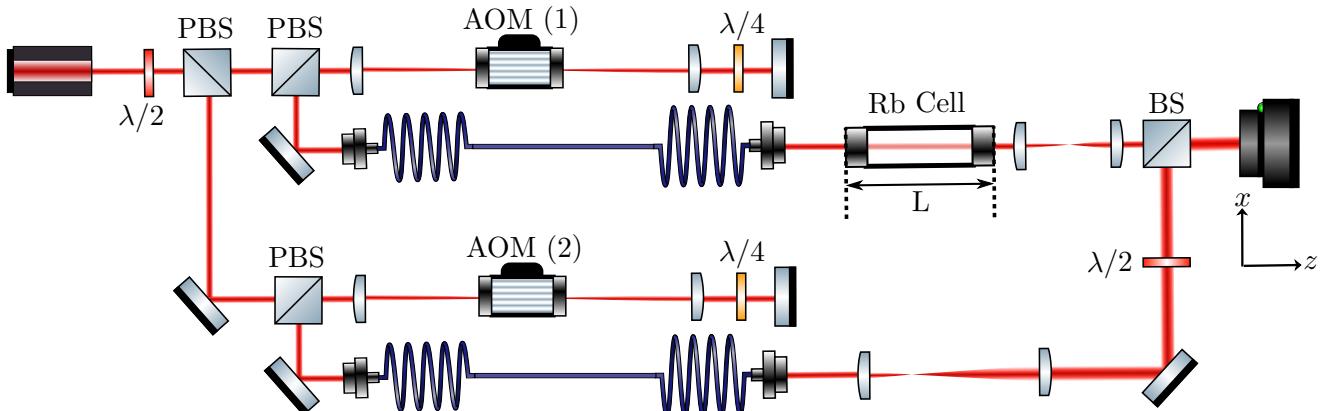
Figure 3.2: Schematic experimental set-up. The reference and signal beam are now separated by the first PBS after the laser. Each one goes through an AOM, placed in a so-called "double-pass" configuration. This is preferable to a single-pass configuration, which has some leak diffraction when it is off. This diffraction leak is enough once integrated over a long time (34 ms) on the camera to blur the signal from the pulse ($\simeq$ 100 ns). For each AOM only the first order diffraction is selected on both crossings.

The AOM can be switched on and off at a rate close to 20 MHz, we can thus control finely the width and delay of the signal and reference pulses. A scheme of the time delays of both pulses is given in figure 3.3a, with a corresponding interferogram in figure 3.3b. On this image the contrast is low ($\simeq$ 0.1) but uniform (no ring is present): we are able to extract the nonlinear phase of the signal, which is linked to the susceptibility, at $t = \tau$.

3.3   Temporal response of the medium

Using the set-up presented in figure 3.2, we retrieve $\Delta n(\tau)$. One measurement is presented in figure 3.4. The data are fitted by an exponential function, with a characteristic time describing the response of our medium.

(a) Intensity of the two pulses

(b) Interferogram, with a low contrast
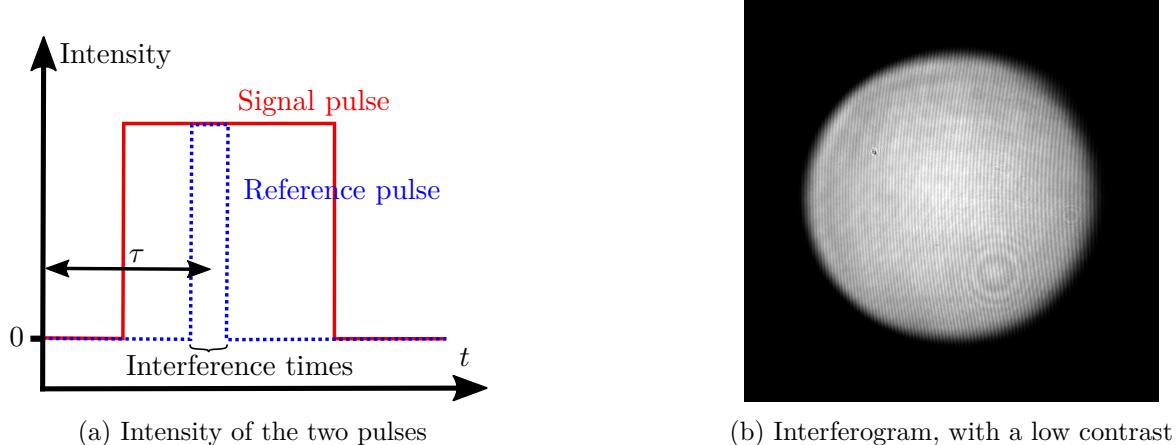
Figure 3.3: (a) Schematic view of the time delay between the two pulses. The reference pulse only overlaps with the signal during a short time window (1/10 the length of the signal pulse). We retrieve the nonlinear phase from the interferogram (b), which is linked to $\chi^{(3)}(\tau)$.

This is to be compared to the numerical simulation of the optical Bloch equations (OBEs) in figure 3.5, where we retrieve the same exponential response behaviour. However, plugging in the experimental parameters of figure 3.4 (and in particular $T = 413\,\mathrm{K}$), the OBEs yield a response time $\tau = 1.7\,\mu\mathrm{s}$. Letting for instance the temperature be a free parameter, it would require $T = 468\,\mathrm{K}$ to recover the response time of $0.95\,\mu\mathrm{s}$ obtained in the experiment. This shows the limitations of our simple atomic model, which is only able to predict a good order of magnitude for this measure. However, it is one of the group's project to improve this model, and one approach currently developed (by Tangui, a phd student) is to realise Monte-Carlo simulations to better take into account the transit of atoms through the beam.
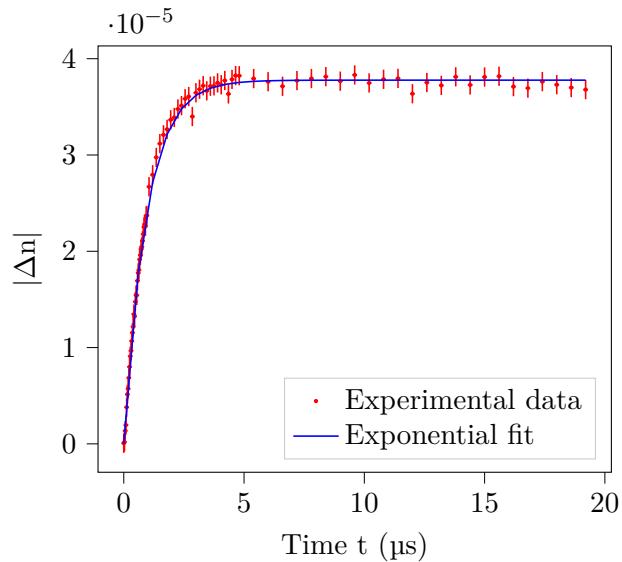
Figure 3.4: Measure of the response of Δn from our medium. For each point we apply the method detailed section 2.2. The result is fitted with an exponential function and we obtain a reponse time $\tau = 0.95\,\mu\mathrm{s}$. Parameters: $\Delta = -7.6\,\mathrm{GHz}$, $w_0 = 660\,\mu\mathrm{m}$, $T = 413\,\mathrm{K}$ and $P = 400\,\mathrm{mW}$.

The scan of the delay between the two pulses allowed us to obtain the nonlinear index change with a very good time resolution, up to $50\,\mathrm{ns}$. We observe that the typical response time is of the order of $1\,\mu\mathrm{s}$, with an exponential response time. This order of magnitude is crucial: pulses of the order of $100\,\mathrm{ns}$ or shorter are needed to have spherical BECs through the analogy of equation (3.1). This means that such pulses will always stay in the transient regime of the susceptibility, unless additional beams are added to pump the medium to its steady-state.

10

(a)

(b)
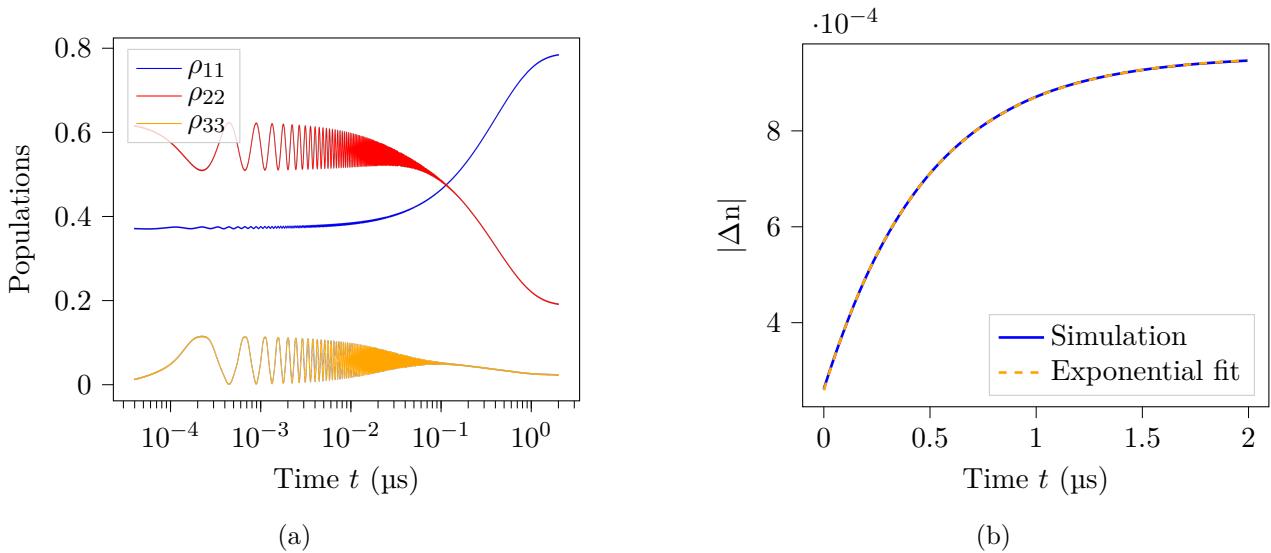
Figure 3.5: Time-dependent OBEs simulation. We represent in (a) the populations: initially the atoms are at rest, the populations are given by the degeneracy rates. We observe some Rabi flopping between the two coupled states $|2\rangle$ and $|3\rangle$ (see figure A.1b), which decays with the optical pumping of the atoms towards the state $|1\rangle$. A steady-state is achieved after a few µs. In (b) we calculate from the coherences the refractive index. We subtract from it the linear index, obtained from a simulation at very low power ($\simeq 10\,\text{nW}$), to extract the nonlinear index Δn (filtered in Fourier space to eliminate high frequencies, not resolvable in the experiment). A characteristic time is obtained by fitting with an exponential function, which yields $\tau = 0.48\,\text{µs}$. The same value is obtained by taking the smallest eigenvalue of the OBEs matrix, which governs the time evolution. Parameters of the simulations: $w_0 = 1\,\text{mm}$, $\Delta = -1\,\text{GHz}$, $P = 500\,\text{mW}$, $T = 415\,\text{K}$.

In this section I have begun to explore the physics of pulsed beams. I have developed an experiment allowing the retrieval of the nonlinear refractive index change across time. It paves the way towards 3D+1 fluids of light, like we have seen with the equation (3.1). Indeed, it is crucial to be able to measure $\chi^{(3)}(t)$ and ideally to control it to fulfill the needs of an experiment. For instance, it is necessary to have pulsed fluids of light for the experiment described in section 5.1, or the one given section 5.2 in the hope to have a 3D optical lattice and launch a fluid of light. In all these cases, the knowledge of the nonlinear refractive index change, hence the speed of sound, is necessary, and the experiment I developed can bring this information.

4   All-optical potential

Until this point, we have used the equation (1.1) without any potential term, that is with $\delta n = 0$. In the Bose-Einstein condensates community however, putting an external potential has been very fruitful, to achieve many physical systems from optical lattices (Grynberg and Robilliard, 2001) to acoustic analogue black holes (Steinhauer, 2016). Being able to control this potential term in our system would open many possibilities, one of which is explored thereafter: after characterising an all-optical potential in section 4.1 we shape it in order to probe superfluidity in section 4.3.

4.1   Study of the potential

To realise an all-optical potential, we would like to move at will the populations from one ground state to another (see figure A.1b). This would change the susceptibility which is proportional to the atomic density of the ground state we address (A.8). One could think of driving simultaneously the same D-line from the ground state $|2\rangle$ as well. However, this lambda (Λ) configuration is likely to induce coherent nonlinear effects (e.g. Electromagnetically Induced Transparency, four-wave mixing). Yet, we would like to tune independently the potential and the main beam. This task seems difficult with two beams addressing the same D-line.

We thus take advantage of the complex D-lines structure of the Rb atom (which, as William D. Phillips would put, is not a two-level atom): we use two beams, one for each D-line, as pictured in figure 4.1b. The

beam on the D2 line ($\simeq 780\,\text{nm}$, which we will call "fluid", addressing the state $|4\rangle$) will have its ground state populations modified by the beam on the D1 line ($\simeq 795\,\text{nm}$, which we will call "defect", addressing the state $|3\rangle$). This configuration had already been used by Truscott et al. (1999) to create an attractive potential ($\delta n > 0$) which guided light. Here the two beams co-propagate in the cell, with the defect "inside" the fluid like it is shown in figure 4.1a.

(a) Two beams in the (x, y) plane   (b) 4-level model
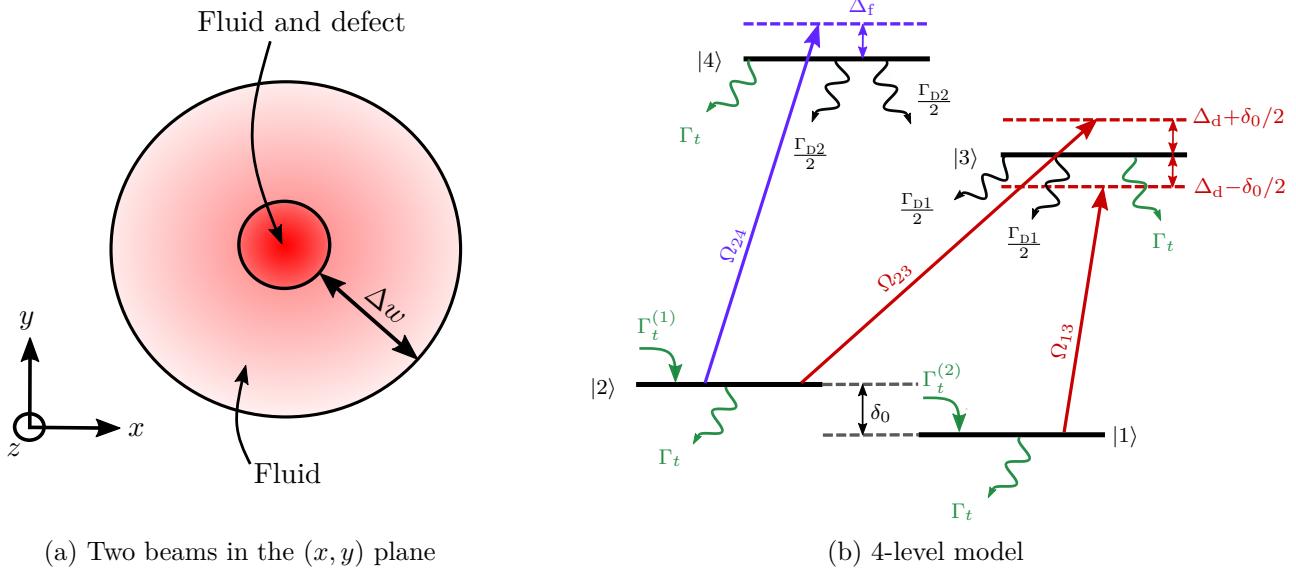
Figure 4.1: (a) Spatial configuration of the two beams, which co-propagate inside the cell. $\Delta w = w_\text{f} - w_\text{d}$ is the approximate distance traveled by atoms through the fluid to reach the defect. Fluid and defect are represented by the blue and red fields respectively in figure (b). This 4-level description is used inside the area where fluid and defect overlap. Otherwise we use the three-level model of appendix A.

With the configuration described in figure 4.1, we can estimate the change of refractive index created by the defect with a simple model developed in Fontaine (2020). We want to evaluate $\delta n = n_\text{f,in} - n_\text{f,out}$ the difference of refractive index seen by the fluid inside and outside of the defect area. $n_\text{f,out}$ is obtained from the model developed in appendix A and $n_\text{f,in}$ from the steady-state solution of the OBE given in appendix E. However, one has to be careful about $\Gamma_t^{(1,2)}$: the atoms do no longer enter the defect area in their natural degeneracy because they have traveled a distance $\Delta w = w_\text{f} - w_\text{d}$ inside the fluid. A fraction α of atoms are prepared in the steady-state. It can be estimated by $\alpha = 1 - \mathrm{e}^{-t_\text{flight}/\tau}$ with $t_\text{flight} = \Delta w / u$, u being the most probable speed of atoms, and $1/\tau$ is the smallest eigenvalue of the OBE matrix (we have seen in section 3 a good agreement of this exponential model with the response of our medium). Therefore:

$$\Gamma_t^{(i)} = \left[(1 - \alpha) G_1 + \alpha \left(\rho_{ii}^\text{f} + \frac{\rho_{44}^\text{f}}{2} \right) \right] \Gamma_t \ , \tag{4.1}$$

with ρ_{jj}^f the steady state solution of the OBE for the fluid only and $G_1 = 3/8$ for ^{87}Rb, the ratio of the degeneracy factor of $|1\rangle$ over the total degeneracy of the whole $5^2 S_{1/2}$ level. Plugging this term into the OBE and inverting numerically the steady-state matrix allows us to calculate the susceptibility felt by the fluid inside the defect. Taking then $\delta n \simeq \frac{1}{2} \text{Re}(\chi_\text{f,in} - \chi_\text{f,out})$, we obtain the figure 4.2a by scanning the detunings of both beams (we only look at $\Delta_\text{f} < 0$ to have a stable fluid with repulsive interactions and avoid filamentation).

The aim is then to measure experimentally the height δn of the defect, by varying several crucial parameters: the detunings of the defect and the fluid, the power and size of the defect. For a given set of parameters, we use once again an interferometric method: we retrieve the phase of the fluid at the output of the cell. For this calibration we use a linear fluid, that is with $\Delta n = 0$, the only phase accumulated by the fluid is therefore linked to the height of the defect, with $\Delta\varphi = k_0 L \, \delta n$. We use cross-polarisation to launch the two beams in the cell (see figure 4.9) to easily discard the defect at the output.

However, the comparison between this model and the experiment (one series of measurements being presented in figure 4.2b) presents several caveats:

- When varying the detuning of the defect, it goes across both atomic resonances ($|1\rangle \to |3\rangle$ and $|2\rangle \to |3\rangle$).

(a) Numerical simulation

(b) Experimental data
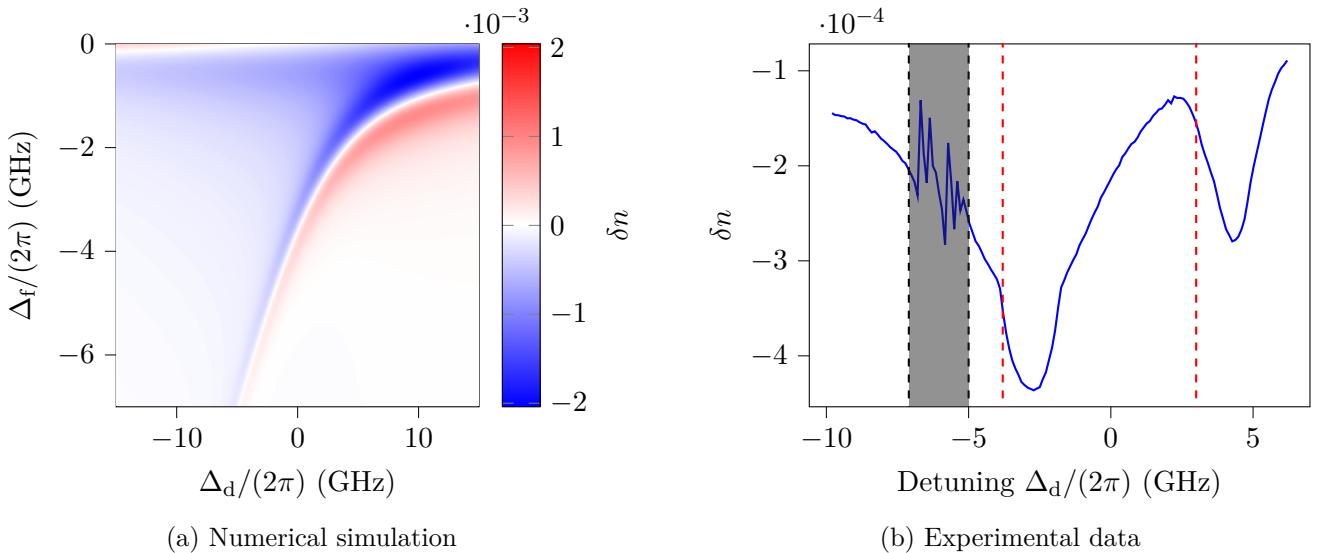
Figure 4.2: (a) Numerical simulation of the height of the defect, varying the detuning of both beams. Parameters: $T = 430\,\mathrm{K}$, $w_\mathrm{f} = 1\,\mathrm{mm}$, $P_\mathrm{f} = 10\,\mathrm{mW}$, $w_\mathrm{d} = 50\,\mathrm{\mu m}$, $P_\mathrm{d} = 200\,\mathrm{mW}$. (b) Experimental measurement of the height of the defect. The comparison with theoretical predictions is difficult to make: the defect size changes due to (de)focusing at certain detunings. The atomic transitions are marked with the red dashed lines. The grey area highlights the zone where a two-photon phenomenon takes place, detailed in appendix E. At these points the data becomes unreliable because no fluid is transmitted in the defect area. Parameters: $T = 430\,\mathrm{K}$, $w_\mathrm{f} = 1.3\,\mathrm{mm}$, $P_\mathrm{f} = 10\,\mathrm{mW}$, $w_\mathrm{d} = 150\,\mathrm{\mu m}$, $P_\mathrm{d} = 350\,\mathrm{mW}$.

Thus, it changes shape across the cell and defocuses (resp. focuses) at the left (resp. right) of the red dashed lines of figure 4.2b.

- We observe a two-photon phenomenon due to a V-configuration of the two beams. This is explained qualitatively in appendix E. Across these detunings, marked with a grey area in figure 4.2b, no fluid is transmitted through the cell in the defect area. It is therefore not possible to retrieve the phase at these points and the data analysis fails.

- The effect of the defect is not limited to the area where the intensity of the beam is high. Indeed, due to atomic diffusion, the ground states of the atoms are changed in a large area around the defect. This creates an effective width of the defect larger than the simple waist of the beam. This effect is discussed in appendix E.

Therefore, the figure 4.2b is difficult to compare with the model presented in figure 4.2a, due to the numerous complications explained above. Yet, the goal during this internship is simply to have a working point where the defect creates a potential energy higher than the kinetic and interaction energies in order to conveniently probe superfluidity. These three energy scales can be estimated starting from the equation (1.1): $E_\mathrm{int} = \hbar c k_0\,|\Delta n|$, $E_\mathrm{pot} = \hbar c k_0\,|\delta n|$, $E_\mathrm{kin} = \hbar c k_0\,\frac{k_\perp^2}{k_0^2}$. We aim at creating a potential such that:

$$|\delta n| \geq |\Delta n| + \underbrace{\frac{k_\perp^2}{k_0^2}}_{=v^2=\beta^2|\Delta n|} \quad \text{for} \quad 0 \leq \frac{k_\perp^2}{k_0^2} \leq |\Delta n| \;, \tag{4.2}$$

with $\beta = v/c_\mathrm{s}$ the Mach number. This inequality means that achieving $|\delta n| \geq 2\,|\Delta n|$ is the right condition to insure that the fluid will not flow over the potential, even when its velocity reaches the sound speed. We typically have $|\Delta n| \simeq 10^{-4}$, therefore placing ourselves at the maximum potential observed in figure 4.2b ($\Delta_\mathrm{d} \simeq -3\,\mathrm{GHz}$) fulfills this condition. To sum up, using the 2 Rb D-lines to create a localised potential comes with several caveats; in particular we have to be careful that changing the detuning or intensity of the fluid beam modifies the potential. However, it enables the creation of a high enough potential ($|\delta n| = 4 \times 10^{-4} \geq 2|\Delta n|$) to probe superfluidity, as we will see in section 4.3.

4.2   Rayleigh scattering

We have seen in the previous section that we
are able to create a localised potential in a
fluid of light. This defect is the ideal tool
to probe the superfluid nature of our fluid
of light. Indeed, as detailed in appendix C,
we are able to define a critical velocity v_c
(through Landau's criterion) which is equal
to the sound velocity c_s for our system. Any
object moving slower than the sound veloc-
ity through the fluid (or conversely the fluid
moving around the object) should therefore
behave in a superfluid manner. In particu-
lar, there should be no scattering of the fluid
of light on this object. We recall that in our
system, thanks to the space-time mapping,
giving a transverse velocity to the fluid sim-
ply means to put it at an angle in the cell,
like illustrated in figure 4.3.

Figure 4.3: Illustrative set-up for this experiment. We launch the
defect and fluid beams in the cell, one with an angle with respect
to the other. This angle acts as a transverse velocity in our 2D+1
formalism.

However, probing superfluidity by looking at the density only is difficult. It has been done by Michel
et al. (2018) by relying on complex observables, such as the displacement of the defect. Hence, we try another
approach: characterising the resonant Rayleigh scattering of the fluid on the defect in Fourier space. This was
theoretically proposed by Carusotto and Ciuti (2004) (for polaritons), Carusotto (2014) (in Kerr media) and
then experimentally realised by Amo et al. (2009) in polaritonic systems. We give in figure 4.4 a detail of the
experimental observation of Rayleigh scattering in our system before discussing the probing of superfluidity in
section 4.3.

(a) Real space

(b) Fourier space

Figure 4.4: Observation of Rayleigh scattering, in real space (a) and in Fourier space (b). The fringes around the path
of the defect in (a) correspond to the Rayleigh scattering ring in (b). This ring, highlighted here with red dashed lines,
is simply a redistribution of momentum around $\mathbf{k} = 0$ (white cross, the momentum of the defect), keeping the norm of
$\mathbf{k}_\perp$ of the fluid (which saturates the camera at this precise momentum). Parameters: $\beta = 0.7$, $T = 394\,\mathrm{K}$, $w_f = 1.7\,\mathrm{mm}$,
$P_f = 790\,\mathrm{mW}$, $w_d = 150\,\mathrm{\mu m}$, $P_d = 27\,\mathrm{mW}$.

Before searching for any superfluid behavior, let us explain in details what are the phenomena at stakes
in figure 4.4. Knowing that the flow is only occurring in one direction, one may wonder about all the density
fringes we observe in figure 4.4a. In fact, when the fluid and the defect enter the cell, the potential and the
interactions are suddenly switched on. From an energetic point of view, the fluid sitting on top of the repulsive
potential is not in a stable position, and it will "roll down" the potential in every direction, creating these

density fringes. We can be more quantitative using the fluid of light formalism: the fluid on top of the potential acquires a phase, proportional to the height of this potential. Besides, we have seen that the velocity of the fluid corresponds to the gradient of its phase, so the fluid will flow according to the gradient of the potential. In our case the potential is a Gaussian, so it will flow in every direction, creating these concentric circles at the right of the defect in figure 4.4a.

As the potential is of Gaussian shape, different parts of the fluid will acquire different different velocities (we remind that a velocity is simply given by $\mathbf{k}_\perp/k_0$ in the paraxial approximation). However, in the case of a nonlinear fluid, most of these excitations will travel at the sound speed due to the Bogoliubov excitation spectrum (see appendix C). Therefore, moving the fluid faster than the sound speed means that the excitations created at the entrance plane will not be able to propagate in the direction opposite to the flow. We then observe a drop in the visibility of the density fringes (inset of figure 4.5a and figure 4.5b). Simultaneously, the Rayleigh scattering ring "opens", meaning that it transforms in a simple circular arc: it is not possible to backscatter light at $-\mathbf{k}_\perp$ because the fluid is moving faster than the velocity of such excitations.

The transition observed in figure 4.5 is thus a signature of the subsonic to supersonic transition of the flow. Yet, this is not linked to superfluidity in our system: due to the finite size of the potential (several times the healing length: $w_\mathrm{d}/\xi \simeq 10$), the superfluid transition will happen around a Mach number $\beta \simeq 0.4$ (Frisch et al., 1992). Qualitatively, the fluid flowing closely around the defect will accelerate compared to the overall flow, leading to a reduced critical velocity.

(a)   (b)
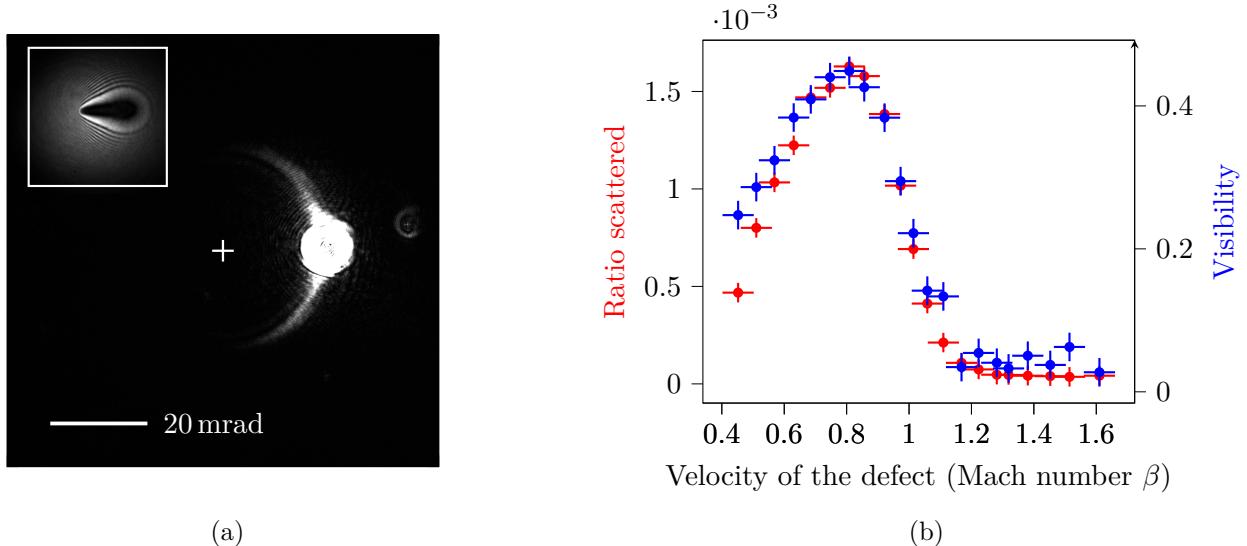
Figure 4.5: (a) Fourier space image of the Rayleigh ring, with $\beta \simeq 1.2$. The inset gives the corresponding real space image. Analysing the ratio of light back-scattered by the defect (which corresponds to the part of the Rayleigh ring at $\mathbf{k} = -\mathbf{k}_\perp$) and the visibility of the fringes when changing the velocity of the fluid, we obtain the figure (b). A clear transition is visible around $\beta \simeq 1$, corresponding to the velocity at which excitations cannot propagate down the flow. Parameters: $T = 394\,\mathrm{K}$, $w_\mathrm{f} = 1.7\,\mathrm{mm}$, $P_\mathrm{f} = 790\,\mathrm{mW}$, $w_\mathrm{d} = 150\,\mathrm{\mu m}$, $P_\mathrm{d} = 27\,\mathrm{mW}$.

Despite the transition shown in figure 4.5, looking at the back-scattered part of the Rayleigh ring (that is $\mathbf{k} = -\mathbf{k}_\perp$) is a good criteria to probe superfluidity. Indeed, the superfluid transition is expected at $\beta \simeq 0.4$ and there is a large range of velocities where we observe a clear Rayleigh scattering (like in figure 4.4b, for which $\beta \simeq 0.7$), and a circular arc is still present when $\beta \geq 1$. However, we need to be careful not to confuse the superfluid regime that we expect with the drop in back-scattering happening at $\beta \simeq 1$.

4.3   Superfluidity?

Giving some velocity to the fluid around a defect, we can probe the normal to superfluid phase transition, which should happen at a Mach number $\beta = v/c_\mathrm{s} = 1$ (for a point-like defect). The experimental path seems pretty clear: changing progressively the velocity of the fluid and keeping the other parameters constant should allow us to probe the transition. Although this is easily done in numerical simulations, like illustrated in figure 4.6, there are several caveats in practice.

(a) $\beta = 1.5$, real space   (b) $\beta = 1.5$, Fourier space   (c) $\beta = 0.4$, real space   (d) $\beta = 0.4$, Fourier space
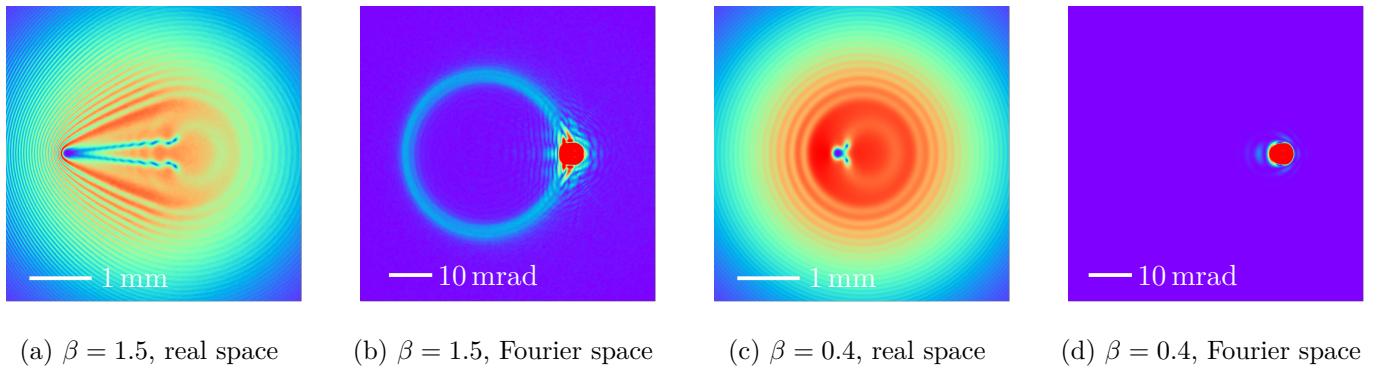
Figure 4.6: 2D+1 NLSE simulations of the experimental configuration of figure 4.3. The Rayleigh ring which is clearly present in (b) disappears in (d), showing the superfluid nature of the fluid for $\beta = 0.4$. However, due to the finite size of the defect, vortex pairs still appear even at low velocities. We notice in (a) a Cerenkov cone appears downstream of the defect. Parameters: $L = 10\,\mathrm{cm}$, $w_\mathrm{f} = 1.5\,\mathrm{mm}$, $w_\mathrm{d} = 30\,\mathrm{\mu m}$, $P = 0.4\,\mathrm{W}$, $n_2 = 2 \times 10^{-10}\,\mathrm{m^2\,W^{-1}}$ and $\delta n = 4 \times 10^{-4}$.

First, we have seen that we expect the superfluid transition to occur at a Mach number $\beta \simeq 0.4$. Indeed, for an impenetrable cylinder as the defect, it has been shown by Frisch et al. (1992) that the critical velocity v_c reduces to $\sqrt{2/11}\,c_\mathrm{s} \simeq 0.42\,c_\mathrm{s}$. Besides, due to its finite size, the defect also generates pairs of vortices. In our system, this allows for the dissipation of energy as we have no viscosity. Eloy et al. (2020) have experimentally tried to map the number of vortices as a function of the defect size. It is also possible to generate pairs of dark solitons (see Maitre et al., 2021, for similar generation of solitons in polaritonic systems), like it is shown in figure 4.7.

Figure 4.7: Observation of a pair of dark solitons, which originate in the flow around the defect. The interferogram highlights the phase shift created by the solitons.

Another caveat also needs to be pointed out: the non-scattered part of the fluid is not a point in Fourier space. Indeed, due to the interactions the fluid defocuses and spreads out in Fourier space (like in figure 4.4b). This spot is even enlarged by the excitations created at the entrance plane when the potential is switched on. It becomes then difficult to distinguish the appearance of the Rayleigh ring which can be close to the unscattered part of the fluid in Fourier space. It is thus crucial to have c_s larger than this part of the fluid in Fourier space, to make sure that the ring can be clearly separated (such as in figure 4.4b).

The aim is then to vary the Mach number β around 0.4 to probe the superfluid transition. It is possible to change v by modifying the angle between the two beams. This has the advantage of keeping the ratios $\delta n/\Delta n$ and w_d/ξ constant. However, it is difficult to identify the position of the Rayleigh ring, which changes for each velocity. On the other hand, when changing β via c_s, the Rayleigh ring stays in the same position. We only need to make sure that the two ratios do not vary extensively, and especially that the condition $\delta n \geq 2\,\Delta n$ is always verified.

This second way of changing β is presented in figure 4.8, allowing us to have a clear diagnosis: we successfully probed the superfluid transition, with the scattering on the defect appearing at $\beta \simeq 0.35$.

Figure 4.8: Transition from a superfluid to a normal fluid, by varying c_s. When the Mach number β increases above a value close to 0.35, the fluid scatters on this potential. Parameters: $w_\mathrm{f} = 0.64\,\mathrm{mm}$, $w_\mathrm{d} = 40\,\mathrm{\mu m}$, $T = 414\,\mathrm{K}$, $\Delta_\mathrm{f} = -1\,\mathrm{GHz}$.
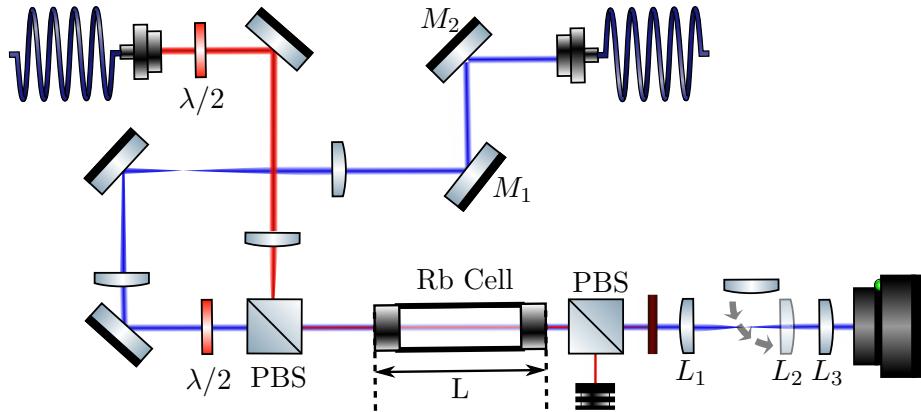
Figure 4.9: Scheme of the experimental set-up. The red beam represents the defect, a lens is used in order to focus it to the right size in the middle of the cell, and it fixes the optical axis. It is discarded at the output thanks to a PBS and a band-pass filter. The blue beam is the fluid. The mirror M_1 is first imaged at the input of the cell, to easily change the angle without touching the position. A telescope images the exit of the cell on the camera. The lens L_2 can be flipped and makes the image of the output of the cell on the lens L_3: the Fourier plane is then captured by the camera.

> Taking advantage of the Rb multiple D-lines, we have seen a way to induce a potential in our medium, thus exploring all the terms of the equation (1.1). I first detailed a simple model to understand how the two beams modify the susceptibility of the atomic vapor, before confronting it to the experimental measurements. We obtained a localised defect with a height δn sufficiently large to create a potential suitable to probe the normal to superfluid transition.
>
> Giving some velocity to the fluid around the defect, we then observed the output state in the real and Fourier space. By understanding quantitatively how the excitations form (in particular in the entrance plane) and propagate, we identify a first interesting transition: the backscattering cancels when the flow goes from subsonic to supersonic, that is at $\beta \simeq 1$.
>
> However, this is not linked to the superfluid transition, which is at $\beta \simeq 0.4$, as expected. By varying β via the sound velocity c_s, we demonstrated the superfluid nature of our fluid of light and probed the normal to superfluid transition.

5 Outlooks

5.1 Black hole horizon

Analogue gravity is a research community which has emerged a few decades ago with the paper of Unruh (1981). He brought forward the analogy between the space-time deformation caused by astrophysical black holes and the equation of motion of sound waves, possibly creating a "sonic black hole". Experiments have followed with evidence of a sonic black-hole horizon shown by Philbin et al. (2008) in an optical fiber and later of Hawking-like radiation in a Bose-Einstein Condensate (Steinhauer, 2016).

Our system exhibits sound waves excitations (see appendix C) and is thus a good candidate to create an analogue black hole. Besides, we have the full control on the velocity at the entrance of the cell: as it corresponds to the gradient of the phase, imposing the phase with a Spatial Light Modulator allows us to tune the input velocity. What are the conditions required to create an analogue black hole? There needs to be a sudden rise in the velocity, accompanied by a drop in the sound speed such that the Mach number of the flow goes from subsonic to supersonic (see figure 5.1a). This situation would create a sonic horizon for phonons in the fluid of light: once in the supersonic region, they can't flow to the subsonic region because they move at c_s in the reference frame of the fluid, and are trapped inside this horizon.

I have confirmed that generating a sonic horizon is feasible in our system, with for instance the configuration shown in the inset of figure 5.1. It takes advantage of the defocusing to have some fluid crossing the horizon created when cutting the beam. The next step in this project would be to observe the Hawking-like radiation once the horizon is achieved. This can be done by measuring the auto-correlation function of the density and detecting a symmetric signal propagating at the speed of sound around the black hole.
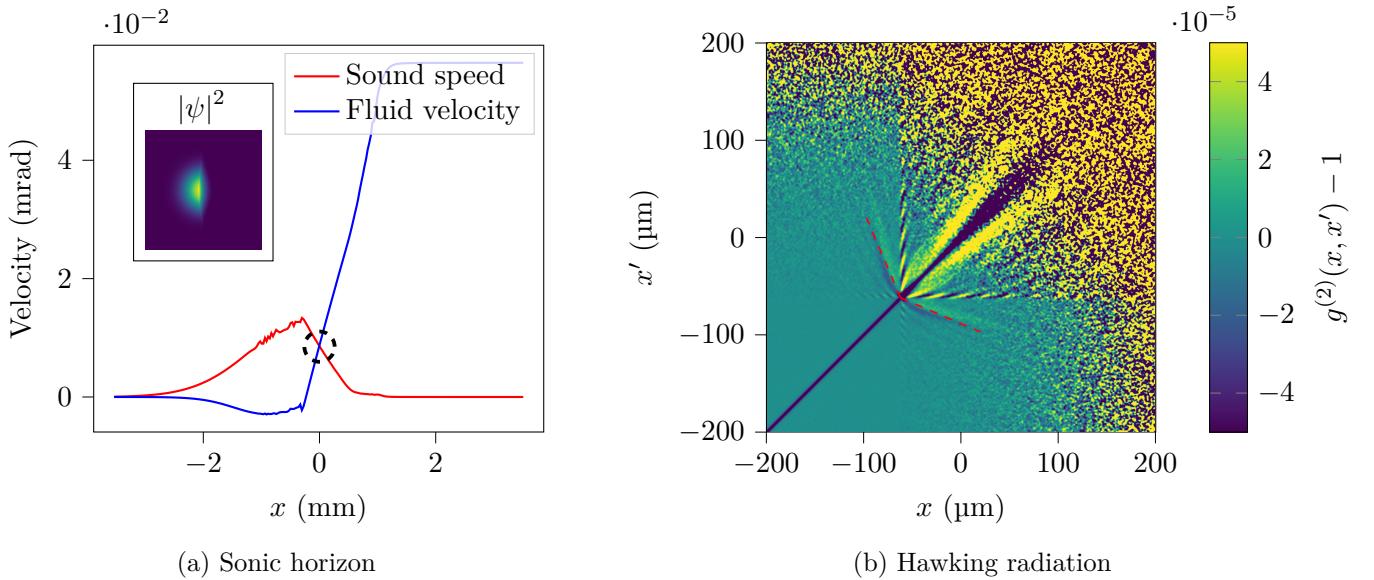
Figure 5.1: (a) Example of a sonic horizon in a 2D+1 NLSE simulation. The inset gives the density, a cut is made at $y = 0$ to look at the velocity and sound speed of the fluid. It goes from subsonic to supersonic, the horizon is circled in black. (b) Correlations of the density, calculated from a 1D+1 GPE simulation in polaritons (simulation made by Malo Joly, another intern of the team). The correlations between Hawking-like particles create a small dip, highlighted here by red-dashed lines.

These quantum fluctuations are however weak and difficult to observe. In order to maximise the signal, it is necessary to increase the analogue temperature, which corresponds in our analogy to the difference of the slopes of the fluid velocity and sound speed (see for instance Barceló et al., 2005). It is then preferable to complete beforehand 2D+1 NLSE simulations with the truncated Wigner approximation (like it is done in figure 5.1b).

Besides, to observe density correlations experimentally we would need to take pictures without any density absorbing filter in front of the camera. This implies to use short pulses (like in section 3) to avoid the saturation of the camera. However, we have seen that the susceptibility of the medium is greatly modified for such pulses. This remains for the moment a major challenge in this project, though studying the time evolution of the susceptibility was a first step towards overcoming this obstacle.

5.2 Optical lattice

Optical lattices in Bose-Einstein Condensates are powerful tools, which allowed the creation of precise atomic clocks (Derevianko and Katori, 2011), and are a fertile ground for quantum simulations (Gross and Bloch, 2017). The realisation of an optical lattice in BECs was first demonstrated by Verkerk et al. (1992). It is realised by placing one (or several) standing waves on top of the condensate, which create periodic potentials for the atoms (see Grynberg and Robilliard, 2001, for a review of the possible potential shapes). These potentials are highly tunable, as their height is simply controlled through the laser intensity. Hence, it becomes possible to reproduce condensed matter Hamiltonians, such as the Bose-Hubbard Hamiltonian, in the tight-binding approximation. One can then probe the Mott insulator to superfluid transition, like it has been done in Greiner et al. (2002).

The realisation and control of optical lattices in our system would therefore allow us to implement many experiments, one example being given in section 5.3. We detail in the following paragraphs some orders of magnitude in order to evaluate the feasibility of an optical lattice, by using the experimental procedure of section 4 to create a potential (which is used in Zhang et al., 2016, for instance). The derivation mainly follows the course given by Dalibard (2013), slightly adapted for fluids of light.

We begin by rewriting the equation (1.1), by setting $\tilde{\mathcal{E}}_0 = \mathcal{E}_0/\sqrt{\int_{\mathbb{R}^2} |\mathcal{E}_0|^2 \, d\mathbf{r}}$ and using the space-time mapping:

$$i\hbar \frac{\partial \tilde{\mathcal{E}}_0}{\partial \tau}(\mathbf{r}_\perp, \tau) = \left[-\underbrace{\frac{\hbar^2}{2(\hbar n_0 k_0/c)}}_{=\hbar^2/(2m)} \boldsymbol{\nabla}_\perp^2 - \underbrace{\hbar c k_0 \, \delta n(\mathbf{r}_\perp, \tau)}_{=\mathcal{V}(\mathbf{r}_\perp, \tau)} - \underbrace{\frac{\hbar c k_0}{2n_0^2} \chi^{(3)}(\omega) \int_{\mathbb{R}^2} |\mathcal{E}_0|^2 \, d\mathbf{r} \, |\tilde{\mathcal{E}}_0(\mathbf{r}_\perp, \tau)|^2}_{=-\hbar c k_0/n_0^2 \times n_2 \mathcal{P} = g} \right] \tilde{\mathcal{E}}_0(\mathbf{r}_\perp, \tau) \, , \quad (5.1)$$

18

with $\mathcal{P} = \frac{1}{2} c \, \epsilon_0 \, n_0 \int_{\mathbb{R}^2} |\mathcal{E}_0|^2 \, \mathrm{d}\mathbf{r}$ the total power of the beam and $n_2 = \frac{1}{\epsilon_0 \, c \, n_0} \chi^{(3)}(\omega)$. Written in this way, we have $\tilde{\mathcal{E}}_0$ with the dimension of an inverse length, as the wavefunction of 2D BECs. Thus, we can use this expression explicitly in the calculations of Dalibard (2013), and in particular the coupling constant g has the same dimension as the one in (1.2).

Starting from the Hamiltonian $\hat{H} = \frac{\hat{p}^2}{2m} + \mathcal{V} + g|\tilde{\mathcal{E}}_0|^2$, the aim is to determine the necessary conditions to recast it into the Bose Hubbard Hamiltonian; and then obtain for a given lattice potential the relative values of the interaction energy U compared to the hopping energy J from one site to another. We will compare these energies to the typical energy scale of the problem, which is the recoil energy $E_{\mathrm{r}} = \frac{\hbar^2 (2\pi/a)^2}{2m}$ (a being the lattice spacing).

Letting the interactions aside for the moment, we take a potential $\mathcal{V}(\mathbf{r}_\perp) = \mathcal{V}_0 \sin\left(\frac{\pi x}{a}\right)^2 + \mathcal{V}_0 \sin\left(\frac{\pi y}{a}\right)^2$, by putting 4 counter-propagating beams for instance, the angle between them fixing the lattice spacing a. We use Bloch's theorem to search for wavefunctions of the form $\tilde{\mathcal{E}}_0 = e^{i\mathbf{q}\cdot\mathbf{r}_\perp} u_{\mathbf{q}}(\mathbf{r}_\perp)$ with $u_{\mathbf{q}}$ a periodic function on our lattice. This simplifies the resolution of the Schrödinger equation to:

$$\hat{H}_{\mathrm{per}}(\mathbf{q}) u_{\mathbf{q}}(\mathbf{r}_\perp) = E(\mathbf{q}) u_{\mathbf{q}}(\mathbf{r}_\perp) \quad \text{with} \quad \hat{H}_{\mathrm{per}}(\mathbf{q}) = \frac{(\hat{p} + \hbar\mathbf{q})^2}{2m} + \mathcal{V}(\mathbf{r}_\perp) \, , \tag{5.2}$$

and $\mathbf{q}$ is restrained to the first Brillouin zone, that is $-\frac{\pi}{a} \leq q_{\mathrm{x,y}} \leq \frac{\pi}{a}$. For each $\mathbf{q}$, there are infinitely many eigenvalues (i.e. energies), which we will classify in increasing order and number by n. The problem is separable into each dimension, so we can write for instance $\tilde{\mathcal{E}}_{n_{\mathrm{x}}}(x, q_{\mathrm{x}}) = \sum_{j \in \mathbb{Z}} C_j(q_{\mathrm{x}}) e^{i(2j\pi/a + q_{\mathrm{x}})x}$, and then solve numerically the eigenvalue equation. In practice we have for each dimension an infinite trigonal matrix, which we restrict to the first terms, giving the figure 5.2a once solved for the eigenvalues. Then, we recover $\tilde{\mathcal{E}}_{\mathbf{n}}(\mathbf{r}_\perp, \mathbf{q}) = \tilde{\mathcal{E}}_{n_{\mathrm{x}}}(x, q_{\mathrm{x}}) \tilde{\mathcal{E}}_{n_{\mathrm{y}}}(y, q_{\mathrm{y}})$.

These Bloch's eigenfunctions form a base of our states. However, they are similar to the base of plane waves in free space, in the sense that they are delocalised over all space. It can be more convenient to use a base which is localised around each potential well, where we will more naturally obtain the energies U and J. This is exactly what the Wannier basis does. Using this basis and switching to the second quantification picture, we obtain the hopping term over j sites in the energy band $n_{\mathrm{x,y}}$:

$$J_{n_{\mathrm{x,y}}}(j) = \frac{a}{2\pi} \int_{-\pi/a}^{+\pi/a} E_{n_{\mathrm{x,y}}}(q_{\mathrm{x,y}}) e^{ijaq_{\mathrm{x,y}}} \, \mathrm{d}q_{\mathrm{x,y}} \, . \tag{5.3}$$

Therefore, $J_{n_{\mathrm{x,y}}}(j)$ only depends on the values of the energies, which themselves vary only with the depth V_0 of the potential. For $\delta n = 10^{-4}$, we can have a deep potential ($V_0/E_{\mathrm{r}} = 10$ like in figure 5.2a) for $a = 200\,\mu\mathrm{m}$. Restricting ourselves to the lower band $\mathbf{n} = 0$, we see that $J_0(1) \gg J_0(j > 1)$: the hopping is restricted to nearest neighbours, and we obtain approximately $J_0(1)/E_{\mathrm{r}} \simeq 0.02$, with $J_0(1) = J$ the hopping amplitude of the Bose-Hubbard model. The term $J_0(0)$ is simply a uniform energy, which we can take equal to 0 by switching the energy reference.

Coming back to the interaction Hamiltonian, and restricting ourselves to the interactions in the lowest energy band and only for atoms on the same sites (the Wannier functions have a negligible overlap between different sites), we obtain:

$$\hat{H}_{\mathrm{int}} \simeq \frac{U}{2} \sum_{\mathbf{j}} \hat{n}_{\mathbf{j}}(\hat{n}_{\mathbf{j}} - 1) \quad \text{with} \quad \frac{U}{E_{\mathrm{r}}} = \frac{2m}{\hbar^2} \frac{g}{2\pi} \sqrt{\frac{V_0}{E_{\mathrm{r}}}} \, , \tag{5.4}$$

after approximating the Wannier function to the first Hermite polynomial, with $\hat{n}_{\mathbf{j}}$ the number of boson on each site. By taking $n_2 = 10^{-10}\,\mathrm{m}^2\,\mathrm{W}^{-1}$ and $\mathcal{P} = 1\,\mathrm{mW}$, we evaluate $U/E_{\mathrm{r}} \simeq 0.5$. Besides, this coefficient is proportional to the power of the beam, so it is easily tunable in our system.
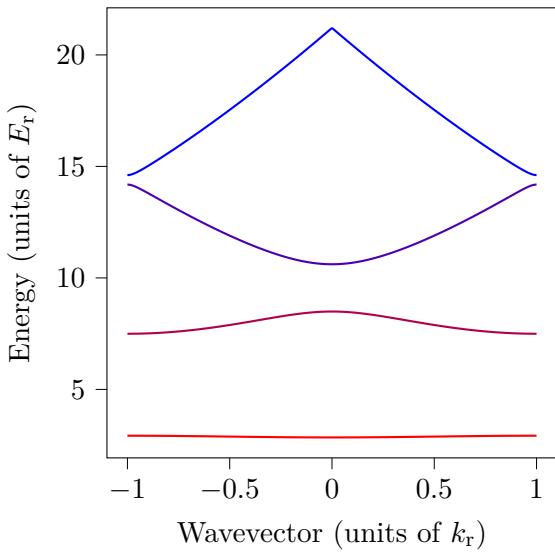
To sum up, the experimental values given above seem promising in the optics of creating a potential lattice in our system (this simple analysis can be extended to pulsed fluids of light to create 3D lattices). Thus, an exciting experimental outlook would be to obtain a system governed by the Bose-Hubbard Hamiltonian, where it would be for instance possible to achieve the Mott insulator to superfluid phase transition.

5.3   Band mapping
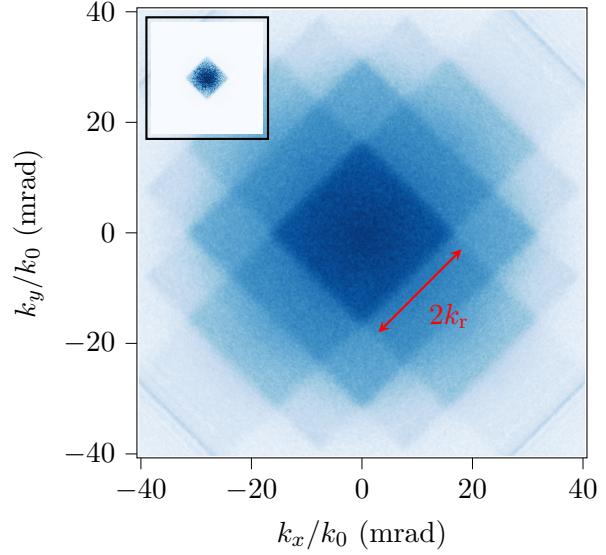
Once we are able to create a potential lattice in our fluid of light, a lot of new experiments may be carried out; one of which would be to realise an optical band mapping (like it has been done by Greiner et al., 2001, in BECs). Indeed, making use of Bloch's theorem we easily see that in such lattices the energy is gaped (such as in figure 5.2a). When the potential lattice is deep, that is when the height V_0 of the potential is much greater than the recoil energy $E_r = \frac{\hbar^2 k_r^2}{2m}$, the width of the first band is much lower than the energy gap between the two first bands.

One can then perform the following steps: load adiabatically a condensate in a lattice potential, to place it at the bottom of the lower band. Then give some kinetic energy to the condensate such that we have $V_0 \gg k_B T \gg E_0$ with E_0 the width of the lowest band. The condensate then occupies uniformly all the energies of the first band, but none in the higher bands. Eventually, unload the condensate and look at its velocity distribution in Fourier space, which directly corresponds to its energy through the band diagram. We obtain some band mapping: the condensate occupies homogeneously all the energies of the first band, and none of it is in the second band, thus the wavevectors in the condensate span exactly the first Brillouin zone.

Therefore, with a square optical lattice, we expect to populate evenly all the momentum of the first Brillouin zone, which is also a square. The far-field figure is thus a perfect square, like it is shown in the inset of figure 5.2b. This is quite remarkable starting with a Gaussian distribution of momentum.

(a) Energy bands

(b) Far field image

Figure 5.2: (a) First four energy bands for a lattice of depth $V_0 = 10 E_r$ over the first Brillouin zone. The width of the lowest band is $0.08 \, E_r$ and the gap between the first and second bands is around $5 \, E_r$. (b) Observation in the Fourier space of the first Brillouin zone through band mapping in a 2D+1 NLSE simulation. The image (b) is in log-scale, allowing us to see the reminescence of several Brillouin zones. The inset is in linear scale and we obtain indeed only the first zone, of width $2k_r$.

In our system, introducing kinetic energy is done by using a speckled beam (see for instance Šantić et al., 2018), which allows us to define an effective temperature in the fluid. However, it is difficult in our case to give this thermal energy after loading the condensate. We therefore chose in this simulation to have the speckle already at the input of the cell, which leaked some fluid in the higher bands but did not impair the main observation.

This exciting outlook faces one major challenge, besides the creation of the optical lattice that we have seen in the previous section. Indeed, it is necessary to load and unload the fluid in this potential. As our effective time evolution corresponds to the z axis, it means that we need to control the height of the potential along the cell. We can imagine taking advantage of the absorption to have a potential varying across z, or control other beams to saturate the medium at some distances, to tune the lattice. In any case this will be a complex task, along with the fine tuning of many parameters to achieve $V_0 \gg k_B T \gg E_0$.

Conclusion

Building up on the analogy between the nonlinear Schrödinger equation describing the propagation of a laser beam in a Kerr medium and the Gross Pitaevskii equation, we can define effective interactions between photons. This contrasts with the propagation of light in vacuum where photons completely ignore each other. Using the Madelung transformation on the NLSE, we obtain hydrodynamic equations, allowing us to better understand the physics at stake by employing a "fluid of light" formalism and the Bogoliubov dispersion relation for small perturbations.

One crucial step in the study of such fluids of light is thus to characterise the interactions between photons. We developed two methods to measure the nonlinearity accumulated by the beam through the cell, one relying on interferometry to exploit the phase of the beam, the other simply looking at its density. Both techniques produced convincing results, and allowed us to confirm the variations of the nonlinear refractive index n_2 with the size of the beam, as predicted by the model of appendix A. A more thorough study of the other parameters of our system (temperature, detuning, isotopic mixture of Rb) is then needed to fully characterise the photon-photon interactions of the Rb hot vapor.

I extended this study to pulsed fluids of light, in order to explore the transient regime of the susceptibility. This step is crucial in the perspective of using 3D+1 fluids of light.

Then, I used a second beam to create an all-optical potential in our system. This was done by taking advantage of the complex D-lines structure of Rb. Shaping this potential in the form of a small defect, I put a flow around this defect to investigate the way it scatters light. This scattering takes the form of resonant Rayleigh scattering and creates a ring in the far-field image of the beam. We were able to identify two clear transitions: from subsonic to supersonic, thanks to the sonic behaviour of the excitations; and a normal fluid to superfluid transition, which happened at a lower Mach number due to the finite size of the defect. This experiment confirmed the superfluid nature of our fluid of light.

I eventually reviewed a few promising outlooks of this system, with the realisation of analogue black holes and optical band mapping, and I illustrated them with 2D+1 NLSE simulations. The easy-to-use Rb cells as well as the fine control of many parameters and the quantum optics tools at our disposal make of this system a great choice to study many-body physics. This internship brought a clearer and more complete understanding of fluids of light, and will hopefully lead to exciting future works.

A Atomic model of the susceptibility

During this internship we addressed the rubidium D-lines, that is the $5^2S_{1/2} \longrightarrow 5^2P_{1/2}$ ($D1$) or the $5^2S_{1/2} \longrightarrow 5^2P_{3/2}$ ($D2$) transitions. These fine levels are splitted into hyperfine levels, whose detailed frequencies are reported in Siddons et al. (2008). A scheme of the ^{87}Rb D-lines is presented in figure A.1a. We immediately notice that the splitting of the ground state is an order of magnitude larger than the splitting of the excited states. This allows us to couple efficiently one of the hyperfine ground state to the whole fine structure of the excited state by taking $\Delta \gg \delta_{\text{hyperfine}}$. Besides, we notice that, for our hot vapors, the Doppler broadening due to the Maxwell distribution of velocities $\mathcal{P}$ is comparable to the hyperfine splitting:

$$\mathcal{P}_{1D}(v_z) = \sqrt{\frac{m}{2\pi k_B T}} \exp\left(-\frac{mv_z^2}{2k_B T}\right) \quad \text{i.e.} \quad \mathcal{P}_{1D}(\omega) = \sqrt{\frac{m}{2\pi k_B T}} \exp\left(-\left(\frac{\omega - \omega_D}{\Delta\omega_D}\right)^2\right), \quad \text{(A.1)}$$

where ω_D is the center frequency of the transition and $\Delta\omega_D/(2\pi)$ the Doppler linewidth. At $T = 400\,\text{K}$, it is equal to $350\,\text{MHz}$, comparable to the hyperfine splitting of the excited states. Combined with the fact that we use $\Delta \gg \delta_{\text{hyperfine}}$, this broadening justifies our three-level model shown in figure A.1b.
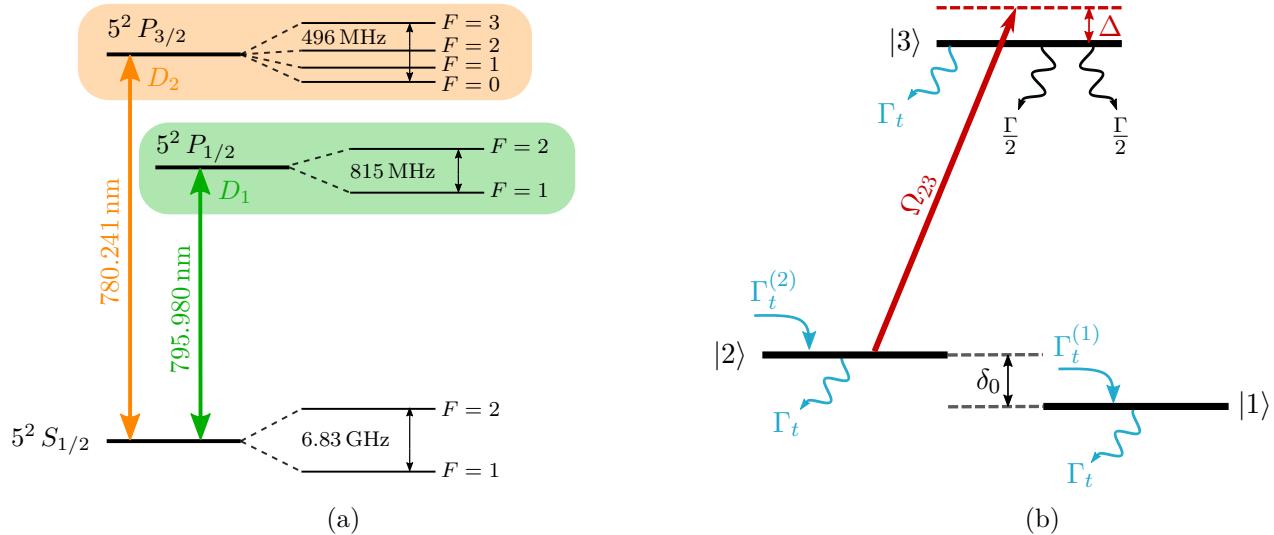

Figure A.1: (a) Atomic levels of the D-lines of ^{87}Rb. The detailed transition values are given in Siddons et al. (2008). When addressing either the $D1$ or the $D2$ line, we can take a three-level model for the Rb lines, as depicted in (b). $|1\rangle$ and $|2\rangle$ correspond to the hyperfine ground state levels and $|3\rangle$ is either the $5^2P_{1/2}$ or $5^2P_{3/2}$ fine level. We have thus $\delta_0 = 6.83\,\text{GHz}$. The blue arrows represent the transit effects induced by the finite size of the beam: atoms enter and exit the beam at a given rate. Γ corresponds to the natural linewidth of the Rb D-lines, for the $D2$ line $\Gamma = 2\pi \times 6.065\,\text{MHz}$.

It is crucial in our system to take into account the finite size of the beam. Indeed, if it were infinite, all the atoms would be pumped in state $|1\rangle$ in the steady-state; there would be no absorption nor any nonlinearity. We introduce Γ_t the transit rate of atoms through the beam (see for instance Sagle et al., 1996). We consider that they enter the beam in their rest steady-state, or in other words that the atom-atom collisions outside the beam repopulate $|1\rangle$ and $|2\rangle$ according to their natural degeneracy. Thus we have $\Gamma_t^{(i)} = \frac{2F_g^i + 1}{8}\Gamma_t$ (8 is the total degeneracy of the $5^2S_{1/2}$ level for ^{87}Rb).

A.1 Density matrix formalism

We work at high intensities, we can therefore adopt a semi-classical approach in order to describe the mean field effects. As such, I will use the density matrix formalism along with the optical Bloch equations in order to retrieve the susceptibility of the medium (I will mainly follow the notations used in Fontaine, 2020, chap. 1). The Hamiltonian is:

$$\hat{H} = \underbrace{\sum_{i=1}^{3} E_i |i\rangle\langle i|}_{\hat{H}_{\text{atom}}} \underbrace{- \hat{\mathbf{d}} \cdot \mathbf{E}(t)}_{\hat{W}(t)} = \hbar\omega_{12}|2\rangle\langle 2| + \hbar\omega_{13}|3\rangle\langle 3| - [(\mathbf{d}_{23}^\star |3\rangle\langle 2| + \mathbf{d}_{23}|2\rangle\langle 3|)\mathcal{E}_0\cos(\omega t)\epsilon], \quad \text{(A.2)}$$

where we have used the dipole approximation to write the atom/field interaction hamiltonian $\hat{W}$, taken the lower state as zero energy and written a continuous monochromatic field $E_0 \cos(\omega t)\epsilon$. We then place ourselves in the interaction picture with respect to the the Hamiltonian $\hat{H}_0 = \hbar\omega \left|3\right\rangle\left\langle 3\right|$, with the aim to get rid of the temporal dependence of the initial Hamiltonian. The unitary transform then writes: $\hat{U} = \exp\left(-i\hat{H}_0 t/\hbar\right)$. By writing $\Omega_{23} = \mathcal{E}_0 \mu_{23}/\hbar$ (with $\mu_{23} = \left\langle 2\right|\hat{\mathbf{d}}\cdot\boldsymbol{\epsilon}\left|3\right\rangle$), we obtain:

$$
\begin{aligned}
\hat{W}_{\mathrm{I}} = \hat{U}\hat{W}\hat{U}^{\dagger} &= -\frac{\hbar}{2}\left(\Omega_{23}^{\star}\mathrm{e}^{i\omega t}\left|3\right\rangle\left\langle 2\right| + \Omega_{23}\mathrm{e}^{-i\omega t}\left|2\right\rangle\left\langle 3\right|\right) \times \left(e^{i\omega t} + e^{-i\omega t}\right) \\
&\simeq -\frac{\hbar}{2}\left(\Omega_{23}^{\star}\left|3\right\rangle\left\langle 2\right| + \Omega_{23}\left|2\right\rangle\left\langle 3\right|\right)\ ,
\end{aligned}
\tag{A.3}
$$

where we make use of the Rotating Wave Approximation when going to the second line. The atomic Hamiltonian commutes with the interaction operator, thus the interaction Hamiltionian reads:

$$
\hat{H}_{\mathrm{I}} = \delta_0 \left|2\right\rangle\left\langle 2\right| - (\Delta - \delta_0)\left|3\right\rangle\left\langle 3\right| - \frac{\hbar}{2}\left(\Omega_{23}^{\star}\left|3\right\rangle\left\langle 2\right| + \Omega_{23}\left|2\right\rangle\left\langle 3\right|\right)\ ,
\tag{A.4}
$$

where δ_0 and Δ are shown in figure A.1b. We can eventually inject (A.4) in the optical Bloch equations (OBEs):

$$
\frac{\mathrm{d}\hat{\rho}_{\mathrm{I}}}{\mathrm{d}t} = -\frac{i}{\hbar}\left[\hat{H}_{\mathrm{I}}, \hat{\rho}_{\mathrm{I}}\right] + \sum_{\nu\neq 0}\left(\tilde{L}_{\nu}\hat{\rho}_{\mathrm{I}}\tilde{L}_{\nu}^{\dagger} - \frac{1}{2}\left\{\tilde{L}_{\nu}^{\dagger}\tilde{L}_{\nu}, \hat{\rho}_{\mathrm{I}}\right\}\right) - \hat{\Gamma}_{\mathrm{t}}\ ,
\tag{A.5}
$$

where I have introduced the Lindblad operators $\tilde{L}_{\nu}$ which take into account the relaxation and decoherence of the atoms and $\hat{\Gamma}_{\mathrm{t}}$ which gathers the relaxation rates due to the finite transit time. We then obtain the following set of equations:

$$
\begin{aligned}
\frac{\mathrm{d}\rho_{11}}{\mathrm{d}t} &= -\Gamma_t\rho_{11} + \frac{\Gamma}{2}\rho_{33} + \Gamma_t^{(1)}\ , \\
\frac{\mathrm{d}\rho_{22}}{\mathrm{d}t} &= -\Gamma_t\rho_{22} + \frac{\Gamma}{2}\rho_{33} + \frac{i}{2}(\Omega_{23}^{\star}\rho_{32} - \Omega_{23}\rho_{23}) + \Gamma_t^{(2)}\ , \\
\frac{\mathrm{d}\rho_{33}}{\mathrm{d}t} &= -(\Gamma_t + \Gamma)\rho_{33} - \frac{i}{2}(\Omega_{23}^{\star}\rho_{32} - \Omega_{23}\rho_{23})\ , \\
\frac{\mathrm{d}\rho_{32}}{\mathrm{d}t} &= -\tilde{\gamma}_{32}\rho_{32} - \frac{i\Omega_{23}^{\star}}{2}(\rho_{22} - \rho_{33})\ ,
\end{aligned}
\tag{A.6}
$$

where $\tilde{\gamma}_{32} = \gamma_{32} - i\Delta = \Gamma/2 + \Gamma_t + \beta N(T)/2 - i\Delta$. The relaxation term $\beta N(T)/2$ corresponds to dephasing dipole-dipole collisions and has been introduced in Weller et al. (2011), Γ is the natural linewidth of the Rb D-lines. We can add the closure relation $\mathrm{Tr}(\hat{\rho}) = 1$, in order to get rid of one of the equations, and rewrite the problem in a matrix form. We can then integrate numerically the resulting system -like it has been done in figure 3.5a- or solve the steady state analytically:

$$
\underbrace{\begin{pmatrix} \Gamma_t + \frac{\Gamma}{2} & \frac{\Gamma}{2} & 0 & 0 \\ \frac{\Gamma}{2} & \Gamma_t + \frac{\Gamma}{2} & -i\frac{\Omega^{\star}}{2} & i\frac{\Omega}{2} \\ i\frac{\Omega}{2} & i\Omega & -\tilde{\gamma} & 0 \\ -i\frac{\Omega^{\star}}{2} & -i\Omega^{\star} & 0 & -\tilde{\gamma}^{\star} \end{pmatrix}}_{M} \underbrace{\begin{pmatrix} \rho_{11} \\ \rho_{22} \\ \rho_{32} \\ \rho_{23} \end{pmatrix}}_{\rho} = \underbrace{\begin{pmatrix} \Gamma_t + G_1\frac{\Gamma}{2} \\ \Gamma_t + G_2\frac{\Gamma}{2} \\ i\frac{\Omega}{2} \\ -i\frac{\Omega^{\star}}{2} \end{pmatrix}}_{X}\ ,
\tag{A.7}
$$

where we have written $\Omega = \Omega_{23}$, $\tilde{\gamma} = \tilde{\gamma}_{23}$ and $G_i = \frac{2F_g^i + 1}{8}$. This system is solved by inverting the matrix M and writing $\rho = M^{-1}\cdot X$ (the detailed expression of ρ can be found in Fontaine, 2020, be careful however to the sign problems in the matrix). We then have a direct access to the polarisability: $P(t) = N\mathrm{Tr}(\hat{\rho}\,\hat{\mathbf{d}}) = 2N\mu_{32}\rho_{32}$. By identifying the susceptibility in the usual expression $P(t) = \epsilon_0\chi\mathcal{E}_0(t)$ (we suppose that the response of the medium is a dirac function), we obtain:

$$
\chi = \frac{G_2 N}{\epsilon_0\hbar}\frac{|\mu_{23}|^2}{\gamma}\frac{i - \Delta/\gamma}{1 + \left(\frac{\Delta}{\gamma}\right)^2 + \left(\frac{\mathcal{E}_0}{\mathcal{E}_{\mathrm{s}}}\right)^2}\ ,
\tag{A.8}
$$

where $\mathcal{E}_\mathrm{s}$ is the saturation field and we have: $\mathcal{E}_\mathrm{s} = \frac{\hbar}{\mu_{23}}\sqrt{\frac{2\Gamma_t(\gamma+\Gamma/2)}{1+\Gamma_t/\gamma}}$. We notice that if $\Gamma_t \ll \Gamma$, we obtain the simple scaling $I_\mathrm{sat} \propto \Gamma_t \propto 1/w_0$ and thus $n_2 \propto w_0$ (the waist of the beam) as discussed in section 2. We have $\Gamma_t/\Gamma \simeq 0.1$ for $w_0 = 100\,\mu\mathrm{m}$ at $T = 430\,\mathrm{K}$, leading thus to the linear scaling of the model in figure 2.3b.

If the condition $\left(\frac{\mathcal{E}_0}{\mathcal{E}_\mathrm{s}}\right)^2 \ll 1 + \left(\frac{\Delta}{\gamma}\right)^2$ is fulfilled, we can expand the expression (A.8):

$$\chi = \underbrace{\frac{G_2 N}{\epsilon_0 \hbar}\frac{|\mu_{23}|^2}{\gamma}\frac{i-\Delta/\gamma}{1+\left(\frac{\Delta}{\gamma}\right)^2}}_{\chi^{(1)}} - \underbrace{\frac{1}{\mathcal{E}_\mathrm{s}^2}\frac{G_2 N}{\epsilon_0 \hbar}\frac{|\mu_{23}|^2}{\gamma}\frac{i-\Delta/\gamma}{\left(1+\left(\frac{\Delta}{\gamma}\right)^2\right)^2}|\mathcal{E}_0|^2}_{\chi^{(3)}} \; , \tag{A.9}$$

which immediately yields the expression of the nonlinear index: $n_2 = \frac{1}{\epsilon_0 n_0 c}\mathrm{Re}\left(\chi^{(3)}\right)$. When the low intensity condition is no longer valid, it is necessary to write the infinite expansion of the susceptibility, which eventually rewrites:

$$\chi = \chi^{(1)} + \frac{\chi^{(3)}|\mathcal{E}_0|^2}{1+\left(\frac{\mathcal{E}_0}{\mathcal{E}_\mathrm{s}}\right)^2\left(1+\left(\frac{\Delta}{\gamma}\right)^2\right)^{-1}} \; . \tag{A.10}$$

In this regime, the equation (1.1) needs to be modified: we add the saturation to the Kerr nonlinearity and the last term on the right-hand side is replaced by: $\frac{\chi^{(3)}|\mathcal{E}_0|^2}{1+|\mathcal{E}_0|^2/|\tilde{\mathcal{E}}_\mathrm{s}|^2}$, with $|\tilde{\mathcal{E}}_\mathrm{s}|^2 = |\mathcal{E}_\mathrm{s}|^2\left(1+(\Delta/\gamma)^2\right)$. This changes the value of the photon-photon interactions and it is necessary to avoid this regime if we want to keep the analogy with the Gross-Pitaevskii equation and BECs.

We have detailed here the optical Bloch equations considering only one coupling field. It would be more correct to consider that the electric field also couples the $|1\rangle \to |3\rangle$ transition. The approach is the same as described above, but involves more equations, which we do not detail here, as they do not provide any physical insight. However, all the simulations involving susceptibilities presented in the main text are done with the two coupling fields.

A.2   Doppler effect

The moving atoms along the optical axis experience a frequency shift of the laser due to the Doppler effect. We can take this effect into account in the calculation above, by convolving the susceptibility with the Maxwell Bolzmann velocity distribution (A.1). It creates a broadening of the susceptibility, which we can write in the following way:

$$\chi_\mathrm{D}(\Delta) = \int_{-\infty}^{\infty}\chi(\Delta - k_0 v)\,\mathcal{P}_\mathrm{1D}(v)\,\mathrm{d}v \; , \tag{A.11}$$

with $\mathcal{P}_\mathrm{1D}$ defined in the equation (A.1). We can evaluate this integral by performing its Fourier transform: the convolution of the two functions becomes a product, and we can evaluate independently $\mathcal{FT}(\chi)$ and $\mathcal{FT}(\mathcal{P}_\mathrm{1D})$. The broadened susceptibility is then obtained by taking the inverse Fourier transform of the product.

I write here only the broadened first order of the susceptibility, which is important for the temperature measurements of our medium (see appendix B). Otherwise we always work far-detuned from the resonance, where the Doppler broadening is negligible. We obtain (using mathematica) for the first order susceptibility:

$$\chi_\mathrm{D}^{(1)}(\Delta) = \chi^{(1)}(0)\,F\left(\frac{\Delta}{k_0 u} + i\frac{\gamma}{k_0 u}\right) \quad \text{with} \quad F(z) = i\sqrt{\pi}\mathrm{e}^{-z^2}\mathrm{Erfc}(-iz) \; , \tag{A.12}$$

and Erfc is the complementary error function, $u = \sqrt{2k_\mathrm{B}T/m}$ the most probable speed. A Voigt profile arises, which is the result of the convolution of a Lorentzian function with a Gaussian one. We will use the formula (A.12) in the following section to obtain the temperature of our medium.

B   Temperature measurement of the Rb cell

The temperature is one of the many we have to change the interactions in our medium. It is therefore crucial to measure it with a good precision, to be able to reproduce the experiments or compare some results with numerical estimations for instance. Even though the temperature varies with a square root in all the formulas of the susceptibility, its main effect is on the density $N(T)$ of atoms in the vapor (typically $N \simeq 10^{19} - 10^{20} \, \mathrm{m}^{-3}$ for our temperatures). This number is an exponential function of temperature (see for instance Siddons et al., 2008) and $\chi \propto N(T)$. Thus, the temperature is a crucial parameter to control the interactions in our medium.

However, retrieving the temperature is not a direct measurement. We determine it from the linear transmission through the cell while scanning the detuning. Using a low intensity beam, such that χ does not depend on I, the intensity at the output of the cell is:

$$I(\mathbf{r}, L) = I_0(\mathbf{r}) \exp\left(-k_0 n_0 \, \mathrm{Im}\left(\chi^{(1)}(\Delta, T)\right) L\right) , \tag{B.1}$$

with I_0 the intensity at the entrance of the cell. This approach is similar to the one used for instance in Weller et al. (2011): they check their model with no fitting parameter by controlling the temperature of their medium. Here we use the same model, but leave the temperature as our only fitting parameter in the formula (B.1). We retrieve the transmission through the cell, which is plotted along with the fit in figure B.1.
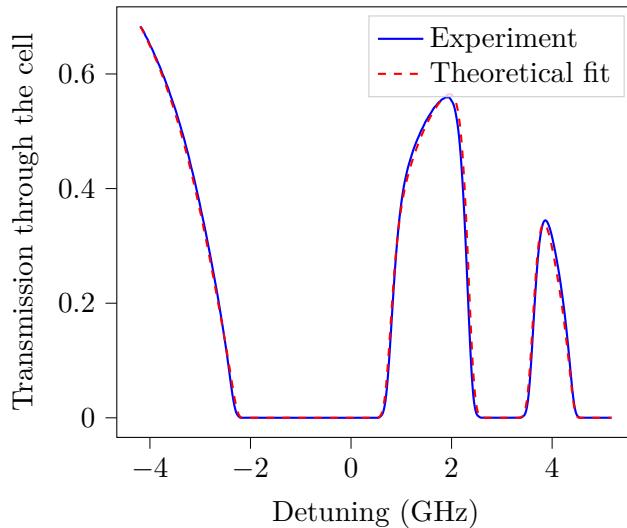

Figure B.1: Linear transmission through the cell, while scanning the laser detuning. Zero detuning corresponds to the $F_g = 3 \to F_e = 2$ hyperfine transition of ^{85}Rb (calibrated with a saturated absorption). The experimental profile is fitted with the model detailed in appendix A by varying the temperature only. It yields here $T = (398 \pm 1) \, \mathrm{K}$ (we typically have T between $380 \, \mathrm{K}$ and $430 \, \mathrm{K}$). The measurements are done with a $10 \, \mathrm{cm}$ long cell of almost isotopically pure (99.2 %) ^{87}Rb.

It is crucial to make this measurement with a very low input power in order to avoid optical pumping and saturation of the medium. In other words, we place ourselves in the limit where the susceptibility is independent of the intensity, which enables us to fit the data with $\chi^{(1)}$ only. In practice, we use an input power around $50 \, \mu\mathrm{W}$, which is a thousand times less than for other experiments.

C   Bogoliubov dispersion relation

Starting from the equation (1.1), we take a situation with $\delta n = 0$ and no absorption. We then perform a Madelung transformation (Madelung, 1926), by writing $\mathcal{E}_0 = \sqrt{\rho(\mathbf{r}_\perp, z)} \, e^{i\phi(\mathbf{r}_\perp, z)}$. We define $\mathbf{v} = \frac{c}{n_0 k_0} \boldsymbol{\nabla}_\perp \phi$ and separate the real and imaginary parts:

$$\frac{\partial \rho}{\partial \tau} + \boldsymbol{\nabla}_\perp (\rho \mathbf{v}) = 0 , \tag{C.1}$$

$$\frac{\partial \mathbf{v}}{\partial \tau} + (\mathbf{v} \cdot \boldsymbol{\nabla}_\perp)\mathbf{v} = \frac{c^2}{n_0^2}\left[\frac{\tilde{n}_2}{n_0}\boldsymbol{\nabla}_\perp \rho + \frac{1}{2k_0^2}\boldsymbol{\nabla}_\perp\left(\frac{1}{\sqrt{\rho}}\boldsymbol{\nabla}_\perp^2 \sqrt{\rho}\right)\right] , \tag{C.2}$$

where we have defined $\tilde{n}_2 = \frac{1}{2n_0}\chi^{(3)}$ and $\tau = \frac{zn_0}{c}$. We would like to establish the dispersion relation of small density modulations over a large uniform background fluid. This will give us some insights on the propagation of density waves in our medium. Thus, we linearise the equations (C.1) and (C.2), by writing $\rho = \rho_0(\tau) + \delta\rho(\mathbf{r}_\perp, \tau)$ and $\mathbf{v} = \mathbf{v}_0(\tau) + \delta\mathbf{v}(\mathbf{r}_\perp, \tau)$, with δ meaning a small perturbation on top of a uniform background fluid. Keeping the first order terms, we obtain:

$$\frac{\partial \delta\rho}{\partial \tau} = -\rho_0 \boldsymbol{\nabla}_\perp \delta\mathbf{v} - \mathbf{v}_0 \boldsymbol{\nabla}_\perp \delta\rho \; , \tag{C.3}$$

$$\frac{\partial \delta\mathbf{v}}{\partial \tau} + (\mathbf{v}_0 \cdot \boldsymbol{\nabla}_\perp)\delta\mathbf{v} = \frac{c^2}{n_0^2}\left(\frac{\tilde{n}_2}{n_0}\boldsymbol{\nabla}_\perp \delta\rho + \frac{1}{4k_0^2\rho_0}\boldsymbol{\nabla}_\perp^3 \delta\rho\right) \; . \tag{C.4}$$

Differentiating the second equation with respect to space and inserting it in the first one yields:

$$\frac{\partial^2 \delta\rho}{\partial \tau^2} + \frac{\partial}{\partial \tau}(\boldsymbol{\nabla}_\perp(\delta\rho) \cdot \mathbf{v}_0) + (\mathbf{v}_0 \cdot \boldsymbol{\nabla}_\perp)\left(\frac{\partial \delta\rho}{\partial \tau} + (\boldsymbol{\nabla}_\perp(\delta\rho) \cdot \mathbf{v}_0)\right) = -\rho_0\frac{c^2}{n_0^2}\left(\tilde{n}_2 \boldsymbol{\nabla}_\perp^2 \delta\rho + \frac{1}{4k_0^2\rho_0}\boldsymbol{\nabla}_\perp^4 \delta\rho\right) \; . \tag{C.5}$$

We use a Fourier decomposition $\delta\rho = A\exp(i\mathbf{q} \cdot \mathbf{r}_\perp - i\Omega z)$. $\mathbf{q}$ is the wavevector of an excitation, which can be created for instance by a probe beam, such as in Fontaine et al. (2018), or a defect like in section 4.2. We then obtain the well-known Bogoliubov dispersion relation:

$$(\Omega(q) - \mathbf{q} \cdot \mathbf{v}_0)^2 = -\rho_0\tilde{n}_2\,q^2 + \frac{1}{4k_0^2}q^4 = -\frac{\Delta n}{n_0}q^2 + \frac{1}{4k_0^2}q^4 \; , \tag{C.6}$$

where $\Delta n = \tilde{n}_2\rho_0 = n_2 I$ is the nonlinear change of refractive index defined in section 2. We first note that Ω is an inverse length in our medium (it usually is a frequency) due to the $z \leftrightarrow \tau$ mapping. This means that velocities can be expressed as angles.

We can identify two regimes in the dispersion relation (C.6), depending on the scale of $1/q$ compared to the healing length $\xi = \frac{1}{k_0}\sqrt{\frac{n_0}{|\Delta n|}}$. This length naturally appears when comparing the two terms of the dispersion relation: $\left(\frac{q^4}{4k_0^2}\right) / \left(\frac{|\Delta n|}{n_0}q^2\right) \sim (q\,\xi)^2$. Thus:

- if $q\,\xi \gg 1$, the dispersion relation becomes quadratic. The excitations have a massive particle-like behaviour.

- if $q\,\xi \ll 1$, the dispersion relation becomes linear. The excitations behave as sound waves and we can define a sound speed $c_\mathrm{s} = \sqrt{\frac{|\Delta n|}{n_0}}$.

The relation (C.6) also allows us to express the Landau criterion for superfluidity in our system. It states that excitations can occur only if they reduce the energy of the condensate, that is if: $\mathbf{q} \cdot \mathbf{v}_0 + \Omega_{\mathbf{v}=0}(q) < 0$, with $\mathbf{v}_0$ the velocity of the fluid compared to a defect (like it is done in section 4). The critical velocity below which no excitation is possible is then given by:

$$v_\mathrm{c} = \min_{\mathbf{q}}\left(\frac{\Omega_{\mathbf{v}=0}(\mathbf{q})}{|\mathbf{q}|}\right) \quad \text{and in our case} \quad v_\mathrm{c} = c_\mathrm{s} \; . \tag{C.7}$$

Below this velocity, no scattering on an obstacle is possible: the flow becomes superfluid. We try to observe this phenomena in section 4.3. We note that for a linear fluid, that is when $\Delta n = 0$, no sonic regime is present and $v_\mathrm{c} = 0$: there exists no superfluid regime.

By casting the equation (1.1) into an adimensionalised form, we can define another typical length for our system, the nonlinear length $z_\mathrm{NL} = (k_0 \Delta n)^{-1}$. We note that ξ and z_NL do not play the same role in our system. ξ emerges from the Bogoliubov dispersion relation, and characterises the evolution of perturbations in the transverse plane (x, y). On the other hand, z_NL indicates an evolution length ($\leftrightarrow$ time) in the z direction. The nonlinear length characterises the time evolution of the fluid through the adimensional relation L/z_NL. For our system the length L is fixed, but we can easily modify the nonlinear length, by changing the intensity of the fluid for instance. This allows us to visualise the nonlinear evolution of the fluid even though we always image the same plane.

D Self defocusing of a gaussian beam

This section merely reproduces some unpublished work done by Nicolas Pavloff, which resulted from a private discussion. We start from the NonLinear Schrödinger Equation for the complex amplitude of the beam $\mathcal{A}(\mathbf{r}, z)$ (with $|\mathcal{A}|^2 = I$ the intensity), and neglect for the moment the linear losses:

$$i\frac{\partial \mathcal{A}}{\partial z} = -\frac{1}{2k_0 n_0}\nabla_\perp^2 \mathcal{A} + k_0 n_2 |\mathcal{A}|^2 \mathcal{A} \ . \tag{D.1}$$

The equation (D.1) has two conserved quantities P_{tot} and P_{E} (corresponding to the power and energy of the beam respectively):

$$P_{\text{tot}} = \int \mathrm{d}^2\mathbf{r}\,|\mathcal{A}|^2 \quad \text{and} \quad P_{\text{E}} = \int \mathrm{d}^2\mathbf{r}\left(\frac{1}{k_0^2 n_0^2}|\nabla_\perp \mathcal{A}|^2 + \frac{n_2}{n_0}|\mathcal{A}|^4\right) \ . \tag{D.2}$$

One then defines the mean square radius of the intensity distribution, which is the observable that we use in section 2.3:

$$\left\langle R^2 \right\rangle (z) = \frac{1}{P_{\text{tot}}}\int \mathbf{r}^2 |\mathcal{A}|^2\,\mathrm{d}^2\mathbf{r} \ . \tag{D.3}$$

We denote with R_0^2 the initial mean square radius. One can then show that (see Landau et al., 1984, § 109 of the 8$^{\text{th}}$ volume):

$$\left\langle R^2 \right\rangle (z) = \frac{P_{\text{E}}}{P_{\text{tot}}}z^2 + R_0^2 \ . \tag{D.4}$$

It is useful in our case to give expressions for P_{E} and P_{tot} for a gaussian beam of the form $\mathcal{A}(\mathbf{r}, z = 0) = \sqrt{I_0}e^{-(x^2+y^2)/w_0^2}$:

$$P_{\text{tot}} = \frac{\pi}{2}I_0 w_0^2 \quad \text{and} \quad P_{\text{E}} = \frac{\pi I_0}{n_0^2 k_0^2} + \frac{\pi}{2}\frac{n_2 I_0^2 w_0^2}{n_0} \ . \tag{D.5}$$

We see that n_2 appears in the expression of P_{E}, showing that it is possible to extract it from the values of $\left\langle R^2 \right\rangle (z)$ knowing all the other parameters (waist, intensity). These calculations therefore prove that it is possible to measure the Kerr nonlinearity from the self-defocusing (focusing) of a gaussian beam.

However, we have not taken into account the linear absorption neither the saturation of the media. Both these corrections can be computed in order to reshape the formula (D.4). However, all the orders of the saturating nonlinearity cannot be calculated analytically, the theoretical profile of $\left\langle R^2 \right\rangle (z)$ is thus false at high intensity (for $I \simeq I_{\text{sat}}$ and higher). The best way to fit the experimental data remains to compare it with 2D+1 NLSE simulations, where all the effects mentioned are easily incorporated.

E Potential in a fluid of light

The model developed in section 4 is detailed here. We first give the optical Bloch equations associated with the four-level configuration of figure 4.1b, and then explain two caveats of the model: the two-photon phenomena we observe at certain detunings and the effective size of the defect that changes due to the diffusion of atoms.

E.1 Optical Bloch Equations

We use the notations of section 4, noticing that $\Omega_{13} = \Omega_{14}$ which we thus call Ω_{d} (idem for the fluid). Under the usual Rotating Wave Approximation and in the interaction picture, the OBEs read:

$$\frac{\mathrm{d}\rho_{11}}{\mathrm{d}t} = -\Gamma_{\text{t,d}}\rho_{11} + \frac{\Gamma_1}{2}\rho_{33} + \frac{\Gamma_2}{2}\rho_{44} + \Gamma_{\text{t,d}}^{(1)} + \frac{i}{2}\left(\Omega_{\text{f}}\rho_{41} - \Omega_{\text{f}}^\star\rho_{14}\right) + \frac{i}{2}\left(\Omega_{\text{d}}\rho_{31} - \Omega_{\text{d}}^\star\rho_{13}\right)$$

$$\frac{\mathrm{d}\rho_{22}}{\mathrm{d}t} = -\Gamma_{\text{t,d}}\rho_{22} + \frac{\Gamma_1}{2}\rho_{33} + \frac{\Gamma_2}{2}\rho_{44} + \Gamma_{\text{t,d}}^{(2)} + \frac{i}{2}\left(\Omega_{\text{f}}\rho_{42} - \Omega_{\text{f}}^\star\rho_{24}\right) + \frac{i}{2}\left(\Omega_{\text{d}}\rho_{32} - \Omega_{\text{d}}^\star\rho_{23}\right)$$

$$\frac{\mathrm{d}\rho_{33}}{\mathrm{d}t} = -(\Gamma_{\text{t,d}} + \Gamma_1)\rho_{33} + \frac{i}{2}\left(\Omega_{\text{d}}^\star\rho_{23} - \Omega_{\text{d}}\rho_{32}\right) + \frac{i}{2}\left(\Omega_{\text{d}}^\star\rho_{13} - \Omega_{\text{d}}\rho_{31}\right)$$

$$\frac{\mathrm{d}\rho_{44}}{\mathrm{d}t} = -(\Gamma_{\text{t,d}} + \Gamma_1)\rho_{44} + \frac{i}{2}\left(\Omega_{\text{f}}^\star\rho_{14} - \Omega_{\text{f}}\rho_{41}\right) + \frac{i}{2}\left(\Omega_{\text{f}}^\star\rho_{24} - \Omega_{\text{f}}\rho_{42}\right)$$

$$\frac{\mathrm{d}\rho_{21}}{\mathrm{d}t} = -\Gamma_{\mathrm{t,d}}\rho_{21} - i\delta_0\rho_{21} + \frac{i}{2}\Omega_{\mathrm{d}}\rho_{31} - \frac{i}{2}\Omega_{\mathrm{d}}^{\star}\rho_{23} + \frac{i}{2}\Omega_{\mathrm{f}}\rho_{41} - \frac{i}{2}\Omega_{\mathrm{f}}^{\star}\rho_{24} \tag{E.1}$$

$$\frac{\mathrm{d}\rho_{31}}{\mathrm{d}t} = -\left(\Gamma_{\mathrm{t,d}} + \frac{\Gamma_1}{2}\right)\rho_{31} + i(\Delta_{\mathrm{d}} - \delta_0)\rho_{31} + \frac{i}{2}\Omega_{\mathrm{d}}^{\star}\rho_{21} - \frac{i}{2}\Omega_{\mathrm{f}}^{\star}\rho_{34} + \frac{i}{2}\Omega_{\mathrm{d}}^{\star}(\rho_{11} - \rho_{33})$$

$$\frac{\mathrm{d}\rho_{32}}{\mathrm{d}t} = -\left(\Gamma_{\mathrm{t,d}} + \frac{\Gamma_1}{2}\right)\rho_{32} + i\Delta_{\mathrm{d}}\rho_{32} + \frac{i}{2}\Omega_{\mathrm{d}}^{\star}\rho_{12} - \frac{i}{2}\Omega_{\mathrm{f}}^{\star}\rho_{34} + \frac{i}{2}\Omega_{\mathrm{d}}^{\star}(\rho_{22} - \rho_{33})$$

$$\frac{\mathrm{d}\rho_{41}}{\mathrm{d}t} = -\left(\Gamma_{\mathrm{t,d}} + \frac{\Gamma_2}{2}\right)\rho_{41} + i(\Delta_{\mathrm{f}} - \delta_0)\rho_{41} + \frac{i}{2}\Omega_{\mathrm{f}}^{\star}\rho_{21} - \frac{i}{2}\Omega_{\mathrm{d}}^{\star}\rho_{43} + \frac{i}{2}\Omega_{\mathrm{f}}(\rho_{11} - \rho_{44})$$

$$\frac{\mathrm{d}\rho_{42}}{\mathrm{d}t} = -\left(\Gamma_{\mathrm{t,d}} + \frac{\Gamma_2}{2}\right)\rho_{42} + i\Delta_{\mathrm{f}}\rho_{42} + \frac{i}{2}\Omega_{\mathrm{f}}^{\star}\rho_{12} - \frac{i}{2}\Omega_{\mathrm{d}}^{\star}\rho_{43} + \frac{i}{2}\Omega_{\mathrm{f}}(\rho_{22} - \rho_{44})$$

$$\frac{\mathrm{d}\rho_{43}}{\mathrm{d}t} = -\Gamma_{\mathrm{t,d}}\rho_{43} + i(\Delta_{\mathrm{f}} - \Delta_{\mathrm{d}})\rho_{43} + \frac{i}{2}\Omega_{\mathrm{f}}^{\star}\rho_{13} + \frac{i}{2}\Omega_{\mathrm{f}}^{\star}\rho_{23} - \frac{i}{2}\Omega_{\mathrm{d}}\rho_{41} - \frac{i}{2}\Omega_{\mathrm{d}}\rho_{42}$$

We do not expect any analytical consideration from (E.1). However the steady-state matrix can easily be numerically inverted to extract the populations or the susceptibility. This was done to produce the figure 4.2a for instance.

E.2   Two-photon phenomena

While scanning the detuning of the fluid, we observe a two-photon phenomena at a certain set of values. This can be explained qualitatively the following way:
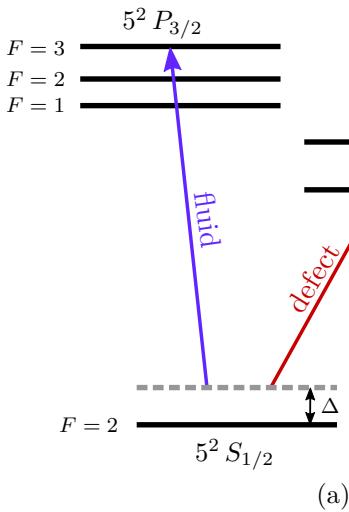
- The defect and fluid have the same detuning from an atomic resonance, each on one of the ^{87}Rb line, like it is shown in figure E.1a.

- The defect (intense compared to the fluid) pumps atoms into of the hyperfine $5^2P_{1/2}$ state, which can be seen in a dressed state-picture as being Δ above the ground state.

- The fluid sees this dressed state and is exactly on resonance with it, and pumps the atoms from $5^2P_{1/2}$ to $5^2P_{3/2}$. It is thus absorbed, and we observe dips in the transmission spectra shown in figure E.1b.

- Six dips are seen when varying the detuning of the fluid. This is due to the hyperfine structure of the Rb atom: the first set of three corresponds to the fluid coupling successively the three hyperfine excited states of the $5^2P_{3/2}$ level and the defect addresses the $F = 1$ level. Indeed, we have seen in figure A.1a that the splitting of the $5^2P_{1/2}$ line is two times higher than that of the $5^2P_{3/2}$ line. Then, the last three dips correspond to the same configuration but with the defect addressing the $F = 2$ level.

This qualitative explanation is supported by two observations. Firstly, the separation of the dips corresponds to the atomic hyperfine splitting that we expect (we measure for instance $830\,\mathrm{MHz}$ between the first and fourth dip, where we would expect $815\,\mathrm{MHz}$). Besides, monitoring the intensity of the defect as well as the one from the fluid, we observe at the same detunings peaks in its transmission spectra: more excited photons are being emitted in a stimulated (and not spontaneous) way thanks to the resonant coupling with the fluid.
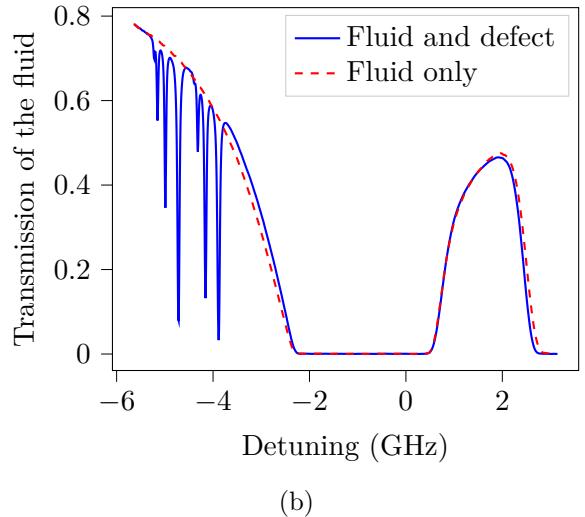
E.3   Effective size of the defect?

The question of the size of the defect is crucial in order to probe superfluidity. Indeed, the ratio w_{d}/ξ (with ξ the healing length, introduced in appendix C) is one of the key parameter to control the phases of the fluid: normal, superfluid, producing vortices or even solitons. This has been experimentally shown in Eloy et al. (2020). One could think that the size of the defect is simply given by the waist of the beam, and that it has a gaussian shape. Yet, due to the ballistic transport of atoms, the proportion of atoms in each of the two ground state changes even outside the defect beam. This has an impact on the susceptibility of the fluid. The mean free path of atoms is given by $l_{\mathrm{c}} = (\sqrt{2}N(T)\sigma)^{-1}$ with σ the collisional cross-section (Skupin et al., 2007). It is shown in Bali et al. (1999) that $\sigma_{\mathrm{g\text{-}g}} = 2.5 \times 10^{-17}\,\mathrm{m}^2$ for collisions in the ground state. It yields $l_c \simeq 1\,\mathrm{mm}$ at $T = 400\,\mathrm{K}$ meaning that an atom exiting from the defect will approximately go through the whole fluid before having a collision that could dephase it and restore a natural proportion in the ground states.

We develop a simple model to take this phenomena into account and verify the orders of magnitude obtained in the experiment: we consider that at a distance r of the defect, a proportion $\frac{1}{\pi}\arcsin\left(\frac{w_{\mathrm{d}}}{r}\right)$ of atoms are prepared

Figure E.1: (a) Scheme of the detuning configuration when a two-photon process is observed. It is responsible for the transmission dips at some precise detunings, like illustrated in (b). The transmission of the fluid with the defect turned off is presented in dashed lines by comparison.

by the defect (we solve the steady-state OBE to obtain the populations of these atoms). Then, the values of $\Gamma_{\text{t,f}}^{(1,2)}$ are modified in the three-level model we solve to obtain the susceptibility in the fluid:

$$\Gamma_{\text{t,f}}^{(i)}(r) = \left[\left(1 - \frac{\theta}{\pi}\right) G_i + \frac{\theta}{\pi}\rho_{ii}^{\text{d}}\right]\Gamma_{\text{t}} \quad \text{with} \quad \theta = \arcsin\left(\frac{w_{\text{d}}}{r}\right). \tag{E.2}$$

Plugging this expression in our atomic model gives the figure E.2a. We obtain a variation of $\delta n \simeq 10^{-4}$, which is coherent with the measures shown in figure E.2b. Besides, we see that the sign of δn changes only at $\Delta_{\text{d}} \simeq 5\,\text{GHz}$, which is once again compatible with the experiment. The variation of index observed in figure E.2b acts like a potential, and should therefore be taken into account when evaluating the height of the defect. However, it becomes difficult in this situation to attribute a numerical value to the size of the defect, which is not simply the waist of the beam. This also complicates the comparison with NLSE simulations, where we need to impose manually the shape of the potential.

E.4   Effect of the fluid on the potential

We noticed that in the scheme 4.1b, the roles of the fluid and the defect are symmetric. Namely, the fluid can also pump atoms from one ground state to the other. It seems therefore reasonable to investigate the influence of the intensity of the fluid on the potential. Numerical simulations indeed confirm that in most cases the intensity of the fluid is a crucial parameter to determine the height of the potential (see figure E.3). This is problematic for several reasons:

- the fluid can be absorbed through the cell, thus changing the height of the potential.

- we would like to change independently the height δn of the potential and the nonlinearity Δn of the fluid, which is tuned with the intensity of the fluid.

We see thanks to the figure E.3 that the height of the potential lessens when the fluid power increases. This can be problematic if we want to probe the superfluid transition by varying c_{s} (and thus the fluid intensity). Indeed, we can imagine the following situation: increasing the fluid power, we see the Rayleigh ring disappear. Would it be due to superfluidity or the potential simply decreasing in height and thus not scattering anymore? In order to avoid this inconvenience, it is crucial to measure the height of the potential to be sure to maintain $\delta n > \Delta n$ (potential energy greater than interaction energy).

In practice, other caveats appear: when the defect is close to an atomic resonance (at $\Delta_{\text{d}} = \pm\delta_0/2$, with δ_0 defined in figure 4.1b) it either focuses (and produce filaments) or defocuses. The only detuning where we managed to observe some Rayleigh scattering is around the crossover of the two hyperfine states (corresponding in this model to $\Delta_{\text{d}} = -\delta_0/2$). Being red-detuned from an hyperfine state and blue-detuned from the other

(a)

(b)
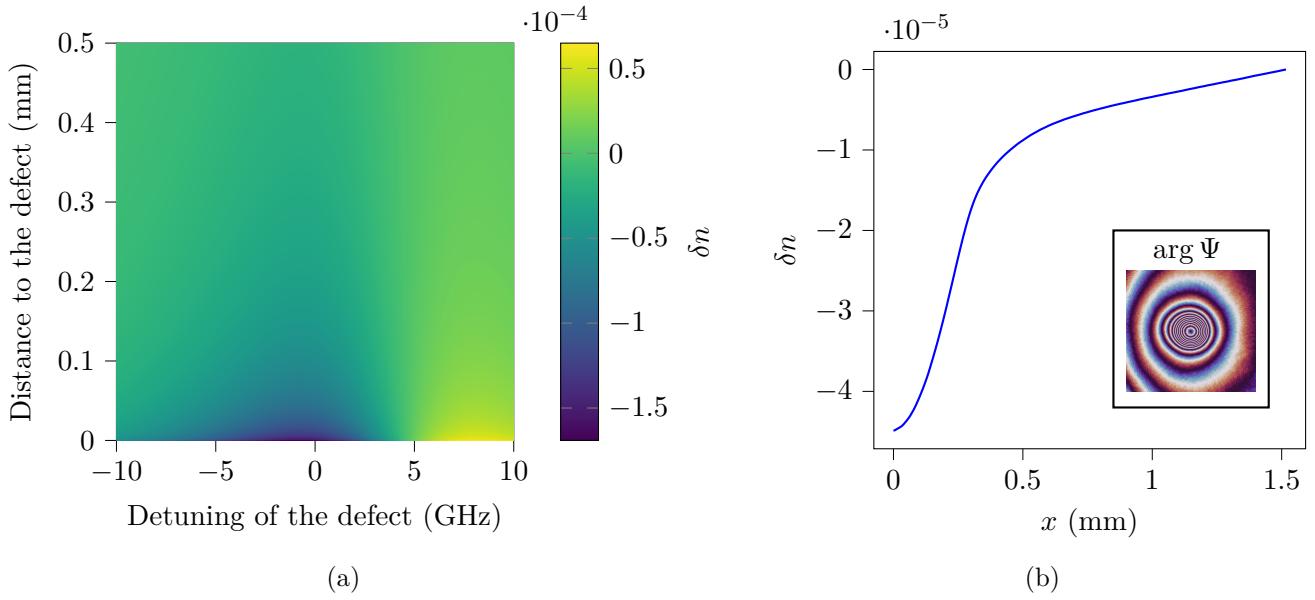
Figure E.2: (a) Numerical simulation of the differential refractive index created by the defect thanks to the ballistic transport of atoms. Parameters: $T = 430\,\mathrm{K}$, $\Delta_\mathrm{f} = -3\,\mathrm{GHz}$, $w_\mathrm{f} = 1.5\,\mathrm{mm}$, $P_\mathrm{f} = 10\,\mathrm{mW}$, $w_\mathrm{d} = 100\,\mu\mathrm{m}$, $P_\mathrm{d} = 400\,\mathrm{mW}$. (b) Azimuthal average of the phase retrieved from an interferogram, with a linear fluid. We clearly observe that a phase shift is present outside of the defect area, meaning that the susceptibility has been changed. Indeed the defect has a waist $w_\mathrm{f} \simeq 0.2\,\mathrm{mm}$ in this image. The inset presents the phase of the fluid, from which we retrieve the azimuthal average.


(a)

(b)
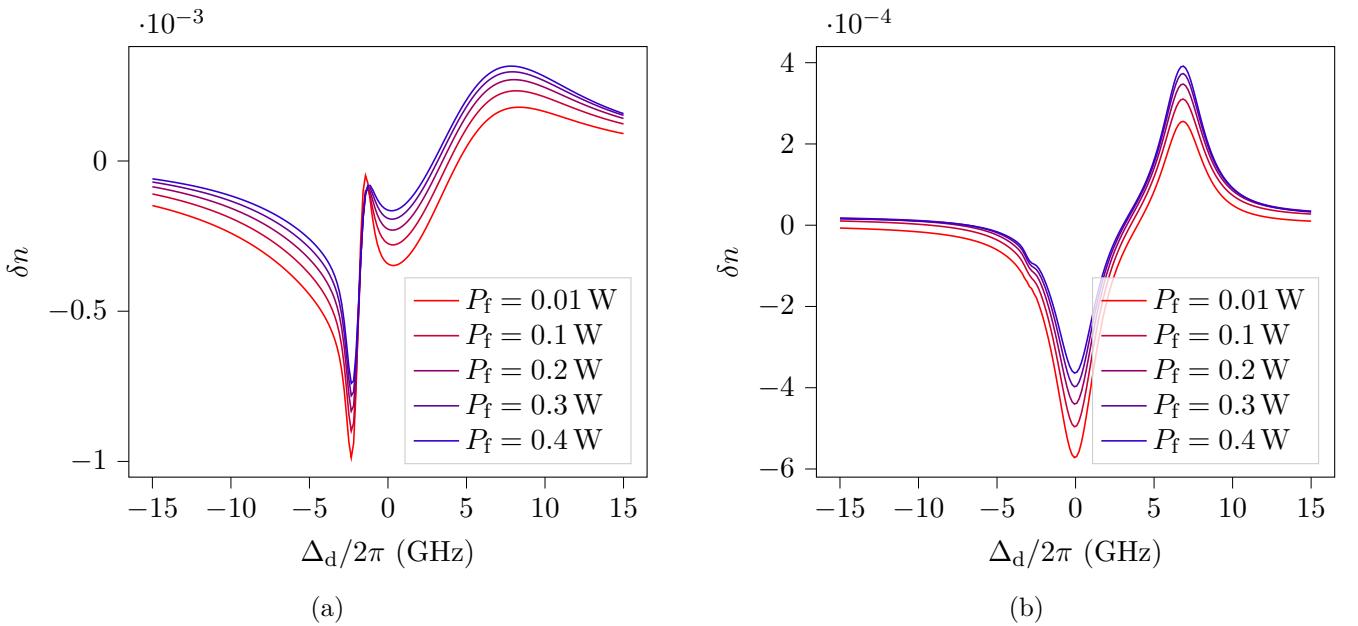
Figure E.3: Numerical simulations of the strength of the potential for several powers of the fluid, and a strong driving defect (a) or a weaker one (b). Parameters: $T = 430\,\mathrm{K}$, $\Delta_\mathrm{f} = -3\,\mathrm{GHz}$, $w_\mathrm{f} = 1.5\,\mathrm{mm}$, $w_\mathrm{d} = 100\,\mu\mathrm{m}$, $P_\mathrm{d} = 400\,\mathrm{mW}$ (a) and $P_\mathrm{d} = 20\,\mathrm{mW}$ (b).

seems to be a good solution to have the defect not changing shape. The detuning being fixed, we then vary the power of the defect to obtain the height of the defect we want, and adjust it when the power of the fluid changes.

References

Abuzarli, M., T. Bienaimé, E. Giacobino, A. Bramati, and Q. Glorieux
  2021. Blast waves in a paraxial fluid of light (a). *Europhysics Letters*, 134(2):24001.

Amo, A., J. Lefrère, S. Pigeon, C. Adrados, C. Ciuti, I. Carusotto, R. Houdré, E. Giacobino, and A. Bramati
  2009. Superfluidity of polaritons in semiconductor microcavities. *Nature Physics*, 5(11):805–810.

Bali, S., K. M. O'Hara, M. E. Gehm, S. R. Granade, and J. E. Thomas
  1999. Quantum-diffractive background gas collisions in atom-trap heating and loss. *Physical Review A*, 60(1):R29–R32.

Barceló, C., S. Liberati, and M. Visser
  2005. Analogue Gravity. *Living Reviews in Relativity*, 8(1):12.

Boyd, R. W.
  2003. *Nonlinear Optics - 3rd Edition*. Elsevier, New York.

Callen, W. R., B. G. Huth, and R. H. Pantell
  1967. Optical patterns of thermally self-defocused light. *Applied Physics Letters*, 11(3):103–105.

Carusotto, I.
  2014. Superfluid light in bulk nonlinear media. *Proceedings of the Royal Society A: Mathematical, Physical and Engineering Sciences*, 470(2169):20140320.

Carusotto, I. and C. Ciuti
  2004. Probing Microcavity Polariton Superfluidity through Resonant Rayleigh Scattering. *Physical Review Letters*, 93(16):4.

Carusotto, I. and C. Ciuti
  2013. Quantum fluids of light. *Review of Modern Physics*, 85:299–366.

Dalibard, J.
  2013. Des cages de lumière pour les atomes : la physique des pièges et des réseaux optiques.

Derevianko, A. and H. Katori
  2011. Colloquium: Physics of optical lattice clocks. *Rev. Mod. Phys.*, 83:331–347.

Eloy, A., O. Boughdad, M. Albert, P.-E. Larré, F. Mortessagne, M. Bellec, and C. Michel
  2020. Experimental observation of turbulent coherent structures in a superfluid of light. *arXiv:2012.13280 [physics]*.

Finot, C., F. Chaussard, and S. Boscolo
  2018. Simple guidelines to predict self-phase modulation patterns. *JOSA B*, 35(12):3143–3152.

Fontaine, Q.
  2020. Paraxial fluid of light in hot atomic vapors. *arXiv:2011.12126 [physics]*.

Fontaine, Q., T. Bienaimé, S. Pigeon, E. Giacobino, A. Bramati, and Q. Glorieux
  2018. Observation of the Bogoliubov Dispersion in a Fluid of Light. *Physical Review Letters*, 121(18):183604.

Fontaine, Q., P.-E. Larré, G. Lerario, T. Bienaimé, S. Pigeon, D. Faccio, I. Carusotto, E. Giacobino, A. Bramati, and Q. Glorieux
  2020. Interferences between bogoliubov excitations in superfluids of light. *Phys. Rev. Research*, 2:043297.

Franken, P. A., A. E. Hill, C. W. Peters, and G. Weinreich
1961. Generation of Optical Harmonics. *Physical Review Letters*, 7(4):118–119.

Frisch, T., Y. Pomeau, and S. Rica
1992. Transition to dissipation in a model of superflow. *Physical Review Letters*, 69(11):5.

Greiner, M., I. Bloch, O. Mandel, T. W. Hänsch, and T. Esslinger
2001. Exploring Phase Coherence in a 2D Lattice of Bose-Einstein Condensates. *Physical Review Letters*, 87(16):160405.

Greiner, M., O. Mandel, T. Esslinger, T. W. Hänsch, and I. Bloch
2002. Quantum phase transition from a superfluid to a Mott insulator in a gas of ultracold atoms. *Nature*, 415(6867):39–44.

Gross, C. and I. Bloch
2017. Quantum simulations with ultracold atoms in optical lattices. *Science*, 357(6355):995–1001.

Grynberg, G. and C. Robilliard
2001. Cold atoms in dissipative optical lattices. *Physics Reports*, 355(5):335–451.

Landau, L., E. Lifshitz, and L. Pitaevskii
1984. *Electrodynamics of Continuous Media - 2nd Edition.* Pergamon press, Moscou.

Larré, P.-E. and I. Carusotto
2015. Propagation of a quantum fluid of light in a cavityless nonlinear optical medium: General theory and response to quantum quenches. *Physical Review A*, 92(4):043802.

Madelung, E.
1926. Eine anschauliche deutung der gleichung von schrödinger. *Naturwissenschaften*, 14(45):1004–1004.

Maitre, A., F. Claude, G. Lerario, S. Koniakhin, S. Pigeon, D. Solnyshkov, G. Malpuech, Q. Glorieux, E. Giacobino, and A. Bramati
2021. Spontaneous generation, enhanced propagation and optical imprinting of quantized vortices and dark solitons in a polariton superfluid: towards the control of quantum turbulence.

Michel, C., O. Boughdad, M. Albert, P.-E. Larré, and M. Bellec
2018. Superfluid motion and drag-force cancellation in a fluid of light. *Nature Communications.*

Philbin, T. G., C. Kuklewicz, S. Robertson, S. Hill, F. König, and U. Leonhardt
2008. Fiber-Optical Analog of the Event Horizon. *Science*, 319(5868):1367–1370.

Piekarski, C., W. Liu, J. Steinhauer, E. Giacobino, A. Bramati, and Q. Glorieux
2021. Measurement of the static structure factor in a paraxial fluid of light using bragg-like spectroscopy. *Physical Review Letters*, 127:023401.

Rodrigues, J. D., J. T. Mendonça, and H. Terças
2020. Turbulence excitation in counterstreaming paraxial superfluids of light. *Physical Review A*, 101(4):043810.

Sagle, J., R. K. Namiotka, and J. Huennekens
1996. Measurement and modelling of intensity dependent absorption and transit relaxation on the cesium line. *Journal of Physics B: Atomic, Molecular and Optical Physics*, 29(12):2629.

Sheik-bahae, M., A. A. Said, and E. W. V. Stryland
1989. High-sensitivity, single-beam n_2 measurements. *Optics Letters*, 14(17):955–957.

Siddons, P., C. S. Adams, C. Ge, and I. G. Hughes
2008. Absolute absorption on rubidium D lines: comparison between theory and experiment. *IOPscience.*

Skupin, S., M. Saffman, and W. Królikowski
2007. Nonlocal Stabilization of Nonlinear Beams in a Self-Focusing Atomic Vapor. *Physical Review Letters*, 98(26):263902.

Steinhauer, J.
2016. Observation of quantum Hawking radiation and its entanglement in an analogue black hole. *Nature Physics*, 12(10):959–965.

Truscott, A. G., M. E. J. Friese, N. R. Heckenberg, and H. Rubinsztein-Dunlop
1999. Optically Written Waveguide in an Atomic Vapor. *Physical Review Letters*, 82(7):1438–1441.

Unruh, W. G.
1981. Experimental black-hole evaporation? *Physical Review Letters*, 46:1351–1353.

Verkerk, P., B. Lounis, C. Salomon, C. Cohen-Tannoudji, J.-Y. Courtois, and G. Grynberg
1992. Dynamics and spatial order of cold cesium atoms in a periodic optical potential. *Phys. Rev. Lett.*, 68:3861–3864.

Weller, L., R. J. Bettles, P. Siddons, C. S. Adams, and I. G. Hughes
2011. Absolute absorption on the rubidium D1line including resonant dipole–dipole interactions. *Journal of Physics B: Atomic, Molecular and Optical Physics*, 44(19):195006.

Zhang, Z., Y. Zhang, J. Sheng, L. Yang, M.-A. Miri, D. N. Christodoulides, B. He, Y. Zhang, and M. Xiao
2016. Observation of parity-time symmetry in optically induced atomic lattices. *Phys. Rev. Lett.*, 117:123601.

Šantić, N., A. Fusaro, S. Salem, J. Garnier, A. Picozzi, and R. Kaiser
2018. Nonequilibrium Precondensation of Classical Waves in Two Dimensions Propagating through Atomic Vapors. *Physical Review Letters*, 120(5):055301.